# We are IntechOpen, the world's leading publisher of Open Access books
# Built by scientists, for scientists

**6,900**
Open access books available

**186,000**
International authors and editors

**200M**
Downloads

Our authors are among the

**154**
Countries delivered to

**TOP 1%**
most cited scientists

**12.2%**
Contributors from top 500 universities

CLARIVATE ANALYTICS
**BOOK CITATION INDEX**
INDEXED

**WEB OF SCIENCE™**

Selection of our books indexed in the Book Citation Index
in Web of Science™ Core Collection (BKCI)

## Interested in publishing with us?
## Contact book.department@intechopen.com

Numbers displayed above are based on latest data collected.
For more information visit www.intechopen.com

# Modeling, Simulation and Experimental Studies of Distortions, Residual Stresses and Hydrogen Diffusion During Laser Welding of As-Rolled Steels

T. Böhme[1,*], C. Dornscheidt[2,*], T. Pretorius[3], J. Scharlack[3] and F. Spelleken[3]
*[1]Freudenberg-Schwab Vibration Control GmbH & Co. KG, Velten b Berlin*
*[2]Strip Processing Lines Division, SMS Siemag AG, Hilden*
*[3]Department Research and Development,*
*Thyssen Krupp Steel Europe AG, Duisburg*
*[*]Formerly with ThyssenKrupp Steel Europe AG*
*Germany*

## 1. Introduction

Beyond the assembling of components laser welding procedures are also increasingly applied in steel manufacturing. Reasons for this trend are: high joining velocities, concentrated heat input resulting in extremely thin heating zones, and nearly constant seam geometries along the welding line. So, for example, welding aggregates are installed at the beginning of electrolytic or hot-galvanizing manufacturing lines to join coils of different thickness or grade for continuous production, cf. Figure 1. To minimize shutdowns welding must be extremely reliable, since the joining zone of the 'endless strip' has to resist high thermal and mechanical loads, such subsequent annealing, bending and tension. Failures lead to technical breakdowns, repairs, and loss of production, which should be avoided as much as possible. Moreover, the welding process must be such robust that material with imperfections, such as oxidations or materials ripples, would be also accurately joined. Welding defects, for instances cracks, pores or seam shrinkages, cf. Figure 2, lead to reduction of the cross-sectional area and, therefore, represent critical regions w. r. t. damage and failure. From the engineering point-of-view it is essential to know, whether residual stresses or heat-induced degradations of the materials strength following from joining become critical or not. This question can be answered by e.g. extensive experimental investigations, during which material combinations, geometries (i.e., thickness) and welding parameters such as joining velocity, welding power or laser caustic are varied. Subsequent tensile tests of the different seams yield the critical strength, which is compared with the loading conditions of the production line.

However, such experiments are time-consuming and, therefore, expensive. Moreover, the derived predictions only hold for the used materials, geometries and investigated process parameters; extrapolations of the results beyond these conditions are not possible. Consequently, it is desirable to have a general framework, which allows for the prediction of the thermal and mechanical material response following from an arbitrary choice of
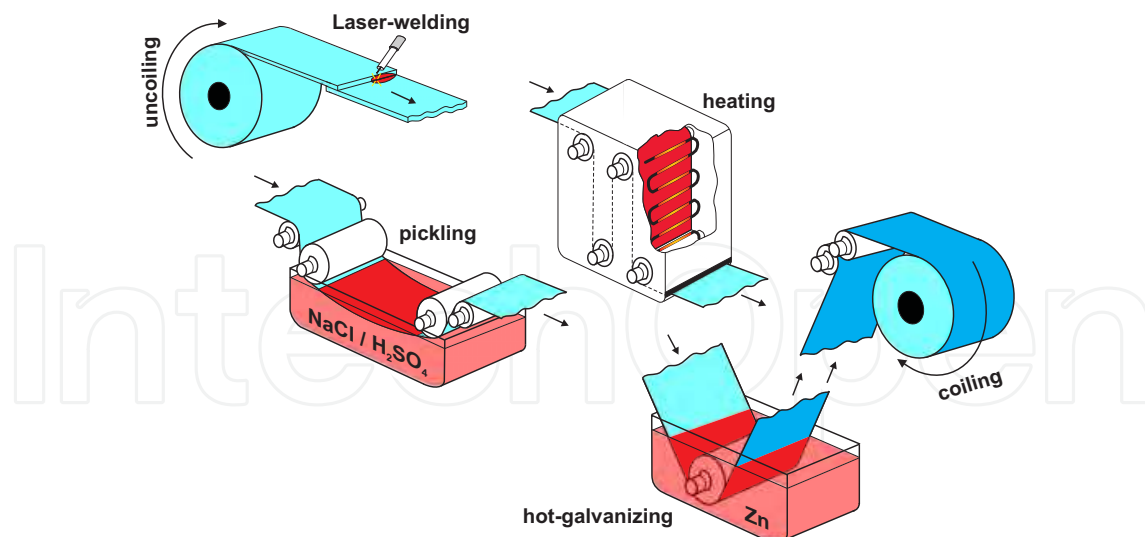
Fig. 1. Illustration of the continuous (hot-)galvanizing process including laser welding at the beginning.

materials, geometries, and welding parameters. Numerical simulations of welding processes increasingly satisfy this demand. They provide information about heat input, resulting thermal distortions, residual stresses or accompanying microstructural changes, and that mostly much faster than corresponding experiments. Thus it is possible to identify critical regions, welding parameters, or materials combinations in advance. In the following
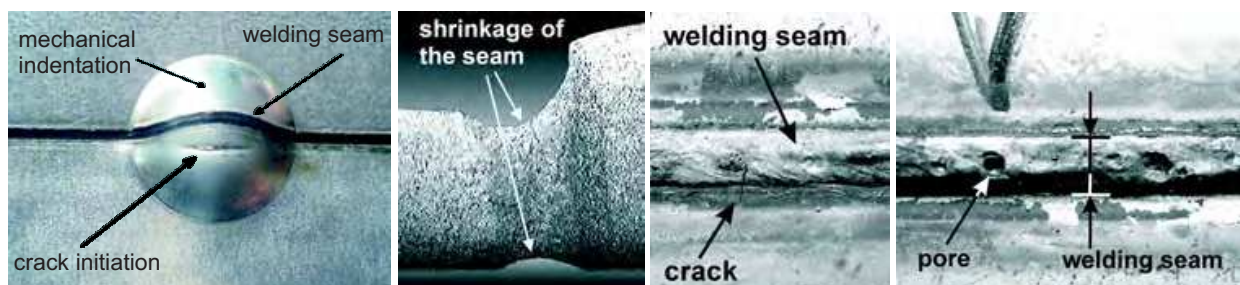


Fig. 2. *Left*: crack initiation within the Heat Affected Zone (HAZ) during the so-called ERICHSEN test. *2nd picture*: shrinkage of the seam at the upper and lower side of two dissimilar sheet geometries. *3rd picture*: Transverse crack due to shrinkage. *Right*: welding pore at the surface of the seam.

sections the laser welding process, with process data typically used during continuous steel manufacturing, will be investigated from the numerical and experimental point-of-view. After an outline to the characteristic continuum-mechanical equations the mathematical framework of Finite Element (FE) simulations is briefly described. Subsequently all required, thermal and mechanical materials data are determined, partially by means of tensile tests with varying temperatures. Different FE simulations are presented using the commercial FE-code ANSYS®, (ANSYS®, 2007), and considering a multiphase TRIP steel (TRIP 700) of 1.8mm thickness. The numerical results are compared with simultaneously performed welding experiments, and,

Modeling, Simulation and Experimental Studies of Distortions,
Residual Stresses and Hydrogen Diffusion During Laser Welding of As-Rolled Steels

77

finally, current limitations, open questions and further tasks for (laser-) welding modelling are discussed.

## 2. A brief review of the physical and mathematical modelling[1]

### 2.1 Thermodynamic states, balances and processes

The thermodynamic state of an arbitrary material point at the position[2] $\underline{x}$ at time $t$ of a system (body) can be completely described by *five field quantities*[3] within the so-called 5-field-theory, viz.

- $\rho(\underline{x}, t)$: mass density,

- $\underline{u}(\underline{x}, t) = \underline{x}(t) - \underline{X}$: displacements,

- $e(\underline{x}, t)$: mass specific internal energy.

$\underline{u}$ represents the displacements of the material point w.r.t. a chosen reference position $\underline{X} = \underline{x}(t_0)$ with (reference) time $t_0$. The internal energy is defined as the difference between total energy and the energy of motion (here: translation), namely $e(\underline{x}, t) = e_{\text{tot}}(\underline{x}, t) - \frac{1}{2}\underline{\dot{x}}^2$.

The temporal and spatial evolutions of the above five fields are determined by so-called *balance equations* (abbr.: balances) for mass, momentum and energy. These equations represent axioms[4] and read:

$$\frac{\partial \rho}{\partial t} + \underline{\nabla} \cdot (\rho \underline{v}) = 0 \, , \tag{1}$$

$$\frac{\partial \dot{\underline{u}}}{\partial t} + \underline{\nabla} \cdot (\rho \underline{v}\, \underline{v} - \underline{\underline{\sigma}}^T) = \underline{f} \, , \tag{2}$$

$$\frac{\partial e}{\partial t} + \underline{\nabla} \cdot (\rho e\, \underline{v} + \underline{q}) = \underline{\underline{\sigma}}^T \cdot \cdot \underline{\nabla}\, \underline{v} + r \, . \tag{3}$$

Please note the identity between the velocity $\underline{v}$ and the time derivative of $\underline{u}$. Furthermore the quantities $\underline{f}$, $\underline{\underline{\sigma}}^T$, $\underline{q}$ and $r$ stand for the sum of externally applied body forces, the transposed CAUCHY stress tensor, the heat flux, and an arbitrary energy production term (e.g. due to latent heat during phase transitions). Eqs. (1-3) are equations of motion for the five unknown fields $\rho$, $\underline{u}$ and $e$. They are universal, namely material-independent. To solve these equations, the *constitutive quantities*, viz. heat flux and stress tensor, must be replaced by constitutive equations (cf. subsequent paragraph) $\underline{q} = \underline{\tilde{q}}(T, \underline{\nabla}T, ...)$ and $\underline{\underline{\sigma}} = \underline{\underline{\tilde{\sigma}}}(T, \underline{u}, ...)$. Moreover, up to now no temperature $T$ occur in the balances (1-3). For this reason a caloric state equation, $e = \tilde{e}(T)$, must be introduced, which allows for replacing the internal energy $e$ by temperature $T$.

---

[1] All considerations refer to Cartesian coordinates. Italic letters stand for scalar values, vectors and tensors of 2nd (or higher) order are characterized by bold and underlined, double underlined (or double underlined with an index of order) letters. Scalar products of vectors and tensors are given by a dot or two dots, respectively.

[2] An EULER-configuration is used in the following considerations, i.e., all equations and quantities refer to the current position; further details can be found in (Gross & Seelig, 2006; Wriggers, 2000).

[3] Field quantities depend on time and position in a continuous and 'sufficiently smooth' (i.e., differentiable) manner, see also (Müller, 1984).

[4] Indeed, the balance for momentum or energy, Eqs. (2, 3), are an alternative formulations of NEWTON's 1st axiom or the 1st law of thermodynamics, respectively, (Müller, 1999; Müller & Müller, 2009).

If all constitutive equations are known and included, the balances represent a closed, coupled and mostly nonlinear System of Partial Differential Equations (PDE), which could be solved (in the majority of cases) by numerical methods. A *thermodynamic process* is defined by the solution of this PDE system, i.e., the knowledge of $\rho$, $\underline{\mathbf{u}}$, and $T$ for all positions $\underline{\mathbf{x}}$ and times $t$. In particular the coupling between mass, momentum and energy - or with other words between materials structure, mechanical and thermal behaviour - lead to the notation of a 'multi-physical process' for welding, cf. Figure 3.
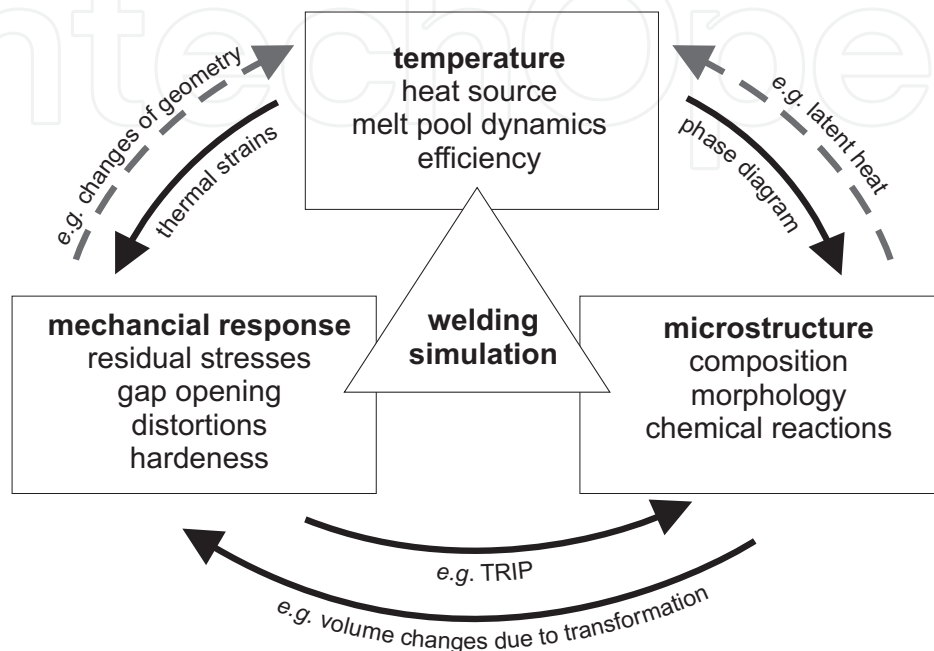


Fig. 3. Interaction of different physical disciplines during welding (dashed indicated couplings are neglected).

## 2.2 Constitutive equations for simulations

Typical constitutive equations, which are provided by commercial FE program packages, such as ANSYS®, are for instances the FOURIER's law of heat conduction:

$$\underline{\mathbf{q}} = -\underline{\underline{\boldsymbol{\kappa}}} \cdot \underline{\boldsymbol{\nabla}} T, \tag{4}$$

the caloric equation of state:

$$\frac{\mathrm{d}e}{\mathrm{d}t} = c_{\mathrm{P}} \frac{\mathrm{d}T}{\mathrm{d}t} \,, \quad (\text{pressure } p = \text{const}) \,, \tag{5}$$

or HOOKE's law for isotropic, elastic solids:

$$\underline{\underline{\boldsymbol{\sigma}}} = \underline{\underline{\boldsymbol{\sigma}}}^{\mathrm{el}} = 2\mu\underline{\underline{\boldsymbol{\varepsilon}}} + \lambda(\mathrm{Tr}\,\underline{\underline{\boldsymbol{\varepsilon}}})\underline{\underline{\mathbf{I}}} - (3\lambda + 2\mu)\underline{\underline{\boldsymbol{\varepsilon}}}^{\mathrm{th}} \,, \tag{6}$$

with with linearized and thermal strains as follows: $\underline{\underline{\boldsymbol{\varepsilon}}} = \frac{1}{2}(\underline{\boldsymbol{\nabla}}\,\underline{\mathbf{u}} + (\underline{\boldsymbol{\nabla}}\,\underline{\mathbf{u}})^{T})$ or $\varepsilon = (x - X)/X$ (for one dimension) and $\underline{\underline{\boldsymbol{\varepsilon}}}^{\mathrm{th}} = \varepsilon^{\mathrm{th}}\underline{\underline{\mathbf{I}}} = \alpha(T - T_0)\underline{\underline{\mathbf{I}}}$. Furthermore the material dependent quantities $\underline{\underline{\boldsymbol{\kappa}}}$, $c_{\mathrm{P}}$, $\lambda$, $\mu$ and $\alpha$ identify the heat conductivity, the specific heat capacity, the LAME's constants, and the thermal expansion coefficient.

Modeling, Simulation and Experimental Studies of Distortions,
Residual Stresses and Hydrogen Diffusion During Laser Welding of As-Rolled Steels

79

A constitutive equation of the form $\underline{\boldsymbol{\sigma}} = \underline{\tilde{\boldsymbol{\sigma}}}(\mathbf{u})$ or $\underline{\boldsymbol{\sigma}} = \underline{\hat{\boldsymbol{\sigma}}}(\underline{\boldsymbol{\varepsilon}})$ for elasto-plastic material behaviour[5], correspondingly to Eq. (6), cannot be derived. The main reasons are **(I)**: there is no mathematical uniqueness for cyclic loading/ unloading, cf. Figure 4 (left), i.e., the appropriate stress for a given strain value depends on the loading history, and **(II)**: the multi-axial stress state and the corresponding strain cannot be directly derived by comparison with the one-dimensional stress-strain curve. To overcome these two items the following strategies are typically applied: **(i)** consideration of increments, which allows taking the loading history into account and **(ii)** introduction of a scalar 'equivalent stress' measure representing the multi-axial state. One of the most established equivalent measures are the VON MISES stress,
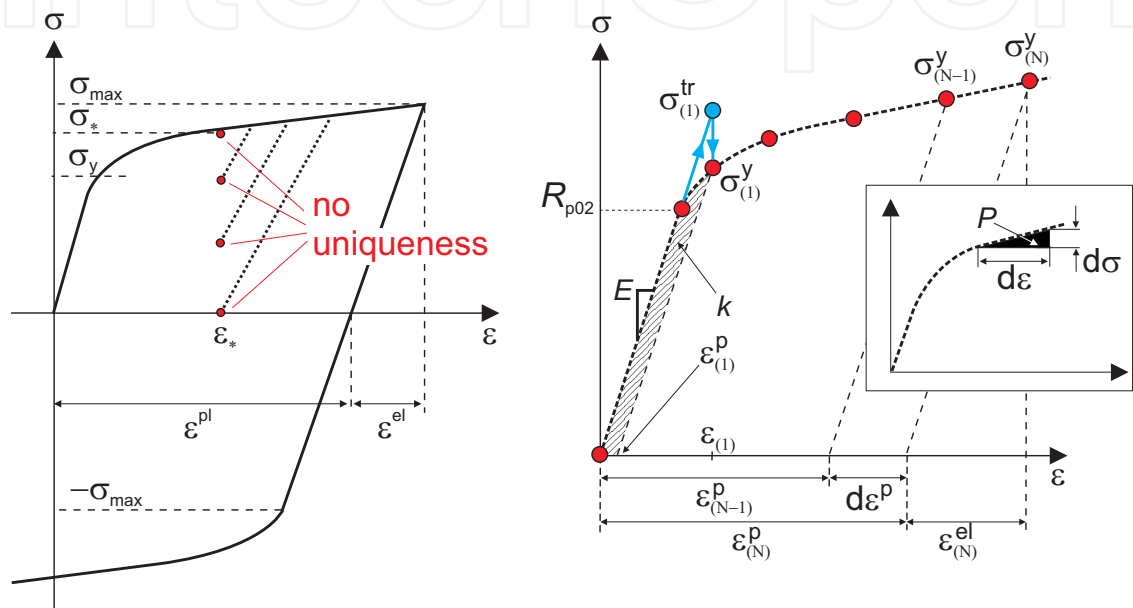


Fig. 4. *Left*: Elasto-plastic (un-)loading including a non-uniqueness regime. *Right*: Illustration of the 1D-stress-strain-curve interpolation, the yield stress calculation and DRUCKER's postulate.

or in the inverse formulation, the VON MISES strain[6]:

$$\sigma_{\mathrm{v}} = \sqrt{\frac{3}{2}\mathrm{dev}\,\underline{\boldsymbol{\sigma}} : \mathrm{dev}\,\underline{\boldsymbol{\sigma}}} \quad \text{and} \quad \varepsilon_{\mathrm{v}} = \sqrt{\frac{2}{3}\underline{\boldsymbol{\varepsilon}} : \underline{\boldsymbol{\varepsilon}}}, \tag{7}$$

where $\mathrm{dev}\,\underline{\boldsymbol{\sigma}} = \underline{\boldsymbol{\sigma}} - p\underline{\mathbf{I}}$ denotes the deviator (i.e., the traceless part) of a tensor, since hydrostatic stresses do not contribute to plastic deformations. By means of a so-called yield criteria, containing the so-called yield-function $\Phi$, it is possible to decide, whether the present stresses lead to yielding or not:

$$\Phi(\underline{\boldsymbol{\sigma}}) = \sigma_{\mathrm{v}}^2(\underline{\boldsymbol{\sigma}}) - \sigma_{\mathrm{y}}^2 = 0 . \tag{8}$$

Here $\sigma_{\mathrm{v}}$ stands for the yield stress, which represents a cylindrical surface in the space spanned by the principle stresses, for details see e.g. (Gross & Seelig, 2006), and which is equal to $R_{\mathrm{p02}}$ for 'virgin' (no strain-hardening) material. If $\sigma_{\mathrm{v}}$, calculated by Eq. (7), is at the surface

---

[5] The following considerations are restricted to time-independent plasticity with isotropic hardening; further models can be found in (Ansys theory ref., 2007).

[6] These quantities are typically used for metals and show realistic results.

or outside of the cylinder yielding will occur; for values inside the cylinder the material will remain elastic.

The yield stress $\sigma_y$ increases with rising plastic deformation, which is called strain-hardening of the material. The mathematical description of this effect follows e.g. by means of a strain-hardening parameter $k$ with $\sigma_y = \tilde{\sigma}_y(k)$ and, therefore, $\Phi(\underline{\sigma}) \rightarrow \Phi(\underline{\sigma}, k)$. For isotropic hardening (Figure 4, right) this parameter is directly linked to the consumed plastic work $P$ of the material via the relation $\dot{k} = \dot{P} = \underline{\sigma} \cdot\cdot \, \underline{\dot{\varepsilon}}^{\mathrm{pl}}$, (Sloan, 1987). Thus the yield condition of Eq. (8) can be used to derive a consistency condition, which - as will be seen subsequently - plays an important role for the determination of the plastic strains. It reads:

$$\dot{\Phi} = \frac{\partial \Phi}{\partial \underline{\sigma}} \underline{\dot{\sigma}} + \frac{\partial \Phi}{\partial k} \dot{k} = 0 \; . \tag{9}$$

The derivative $\partial \Phi / \partial \underline{\sigma}$ follows from Eq. (7) and the expression $\partial \Phi / \partial k$ results from the graphical exploitation of the material specific, temperature-depending, one-dimensional stress-strain curves, cf. Figure 4 (right), provided by the user of the FE program package. The remaining variables $\underline{\dot{\sigma}}$ and $\dot{k}$ can be calculated by HOOKE's law in combination with an additive decomposition of the total strains into an elastic and plastic part, $\underline{\varepsilon} = \underline{\varepsilon}^{\mathrm{el}} + \underline{\varepsilon}^{\mathrm{pl}}$ ($\underline{\underline{C}}_4$ denotes the 4th order stiffness matrix):

$$\underline{\dot{\sigma}} = \underline{\underline{C}}_4 \cdot\cdot (\underline{\dot{\varepsilon}} - \underline{\dot{\varepsilon}}^{\mathrm{pl}}) \quad \text{and} \quad \dot{k} = \underline{\underline{C}}_4 \cdot\cdot (\underline{\dot{\varepsilon}} - \underline{\dot{\varepsilon}}^{\mathrm{pl}}) \cdot\cdot \, \underline{\dot{\varepsilon}}^{\mathrm{pl}} \; . \tag{10}$$

By knowledge of the total strain the only remaining unknown variable is $\underline{\varepsilon}^{\mathrm{pl}}$. In other words, the decomposition of $\underline{\varepsilon}$ into an elastic and plastic part must be determined, see Figure 4. For this reason DRUCKER's postulate[7] can be used, which yields, inter alia, an associated flow rule as follows:

$$\underline{\dot{\varepsilon}}^{\mathrm{pl}} = \dot{\Lambda} \frac{\partial \Phi}{\partial (\mathrm{dev}\,\underline{\sigma})} \quad \text{or} \quad \mathrm{d}\underline{\varepsilon}^{\mathrm{pl}} = \mathrm{d}\Lambda \frac{\partial \Phi}{\partial (\mathrm{dev}\,\underline{\sigma})} \; . \tag{11}$$

Obviously the plastic strains are parallel to the derivative of the yield function w.r.t. the deviator of the stress tensor. The coefficient $\mathrm{d}\Lambda$ characterizes the absolute value of $\mathrm{d}\underline{\varepsilon}^{\mathrm{pl}}$ and must be iteratively determined by means of the consistency condition, cf. (Ansys theory ref., 2007).

Finally a schematic chronology for the computational calculation of the elastic-plastic stresses by means of the above equations is given. Here the total strains (following e.g. by thermal expansion due to heat supply) are assumed to be known:

**(1)** Consideration of the total strains as the sum of temporally successive strains, $\underline{\varepsilon} = \sum_n \underline{\varepsilon}(n)$, representing the deformation history.

---

[7] The postulate states, that for stable yielding the consumed plastic work is always positive (or zero), viz.

$$\mathrm{d}P = \mathrm{d}\underline{\sigma} \cdot\cdot \, \mathrm{d}\underline{\varepsilon}^{\mathrm{pl}} \geq 0 \; ,$$

cf. Figure 4 (right) or explanations in various textbooks, for example in (Stouffer & Dame, 1996). By decomposition of $\mathrm{d}\underline{\sigma} = \mathrm{d}\underline{\sigma}^{\perp} + \mathrm{d}\underline{\sigma}^{\parallel}$ into a normal and tangential part w. r. t. the yielding surface one can geometrically proof, that $\mathrm{d}\underline{\varepsilon}^{\mathrm{pl}}$ is parallel to $\partial \Phi / \partial \underline{\sigma}$ or $\partial \Phi / \partial (\mathrm{dev}\,\underline{\sigma})$, respectively. As a consequence of this fact Eq. (11) directly follows.

Modeling, Simulation and Experimental Studies of Distortions,
Residual Stresses and Hydrogen Diffusion During Laser Welding of As-Rolled Steels

81

**(2)** Calculation of a trial stress by applying HOOKE's law for the $n$-th step as follows[8]:

$$\underline{\underline{\sigma}}^{\mathrm{tr}}(n) = \underline{\underline{C}}_4 \cdot \cdot \left[\underline{\underline{\varepsilon}}(n) - \underline{\underline{\varepsilon}}^{\mathrm{pl}}(n-1)\right] , \tag{12}$$

which - in turn - can be used to compute the equivalent stress $\sigma_{\mathrm{v}}^{\mathrm{tr}}(n)$ according to Eq. (7).

**(3)** Determination of the yield stress $\sigma_{\mathrm{y}}$ by means of the known, material-specific stress-strain-curve and $\underline{\underline{\varepsilon}}^{\mathrm{pl}}(n-1)$. If $\underline{\underline{\varepsilon}}^{\mathrm{pl}}(n-1) = 0$, then $\sigma_{\mathrm{y}}$ will be equal to $R_{\mathrm{p02}}$, otherwise its determination follows from the graphical exploitation according to Figure 4 (right).

**(4)** If the equivalent stress - calculated in the second item - is outside of the yielding surface, then plastic deformations will occur. During this process the plastic strains will reduce the corresponding stresses such that the yield criteria of Eq. (8) will finally hold. Consequently, $\underline{\underline{\sigma}}^{\mathrm{tr}}$ must be projected onto the yielding curve, which is done by adjusting $\mathrm{d}\underline{\underline{\varepsilon}}^{\mathrm{pl}}$, i.e., by varying the factor $\mathrm{d}\Lambda$ within the consistency condition of Eq. (9) and subsequent insertion into Eq. (11).

**(5)** Update of plastic and elastic strains:

$$\underline{\underline{\varepsilon}}^{\mathrm{pl}}(n) = \underline{\underline{\varepsilon}}^{\mathrm{pl}}(n-1) + \mathrm{d}\underline{\underline{\varepsilon}}^{\mathrm{pl}} \quad \text{and} \quad \underline{\underline{\varepsilon}}^{\mathrm{el}}(n) = \underline{\underline{\varepsilon}}(n) - \underline{\underline{\varepsilon}}^{\mathrm{pl}}(n) . \tag{13}$$

**(6)** Calculation of current stresses by:

$$\underline{\underline{\sigma}}(n) = \underline{\underline{C}}_4 \cdot \cdot \underline{\underline{\varepsilon}}^{\mathrm{el}}(n) . \tag{14}$$

**(7)** Continuation with items (2) - (6) for the next steps $(n+1)$, $(n+2)$, etc. .

### 2.3 The principle of finite element analysis

To solve the PDE system following from the balances and the inserted constitutive equations different numerical methods can be applied, e.g. the Finite Element Method (FEM), for details see in various publications and textbooks, e.g. (Dean & Hidekazu, 2006; Kang & Im, 2007; Voss, 2001; Wriggers, 2000). For this reason, today a multitude of commercial programs, such as ANSYS® (ANSYS®, 2007), are available. They provide to the materials engineer a powerful mathematical framework, which conveniently select and solve the problem-specific equations under almost arbitrary conditions. However, a sovereign handling of these programs presumes knowledge about the underlying principles and framework. Therefore a brief explanation about the FEM will be given in the following paragraph. Starting point is the arbitrary PDE of *balance type* for a general scalar quantity $w$:

$$R(\underline{x}, t) = \frac{\partial w(\underline{x}, t)}{\partial t} + \underline{\boldsymbol{\nabla}} \cdot \underline{\tilde{\mathbf{f}}}[w(\underline{x}, t)] - s(\underline{x}, t) = 0 . \tag{15}$$

Here $s$ denotes an arbitrary production or supply and $\underline{\tilde{\mathbf{f}}}$ identifies a vector function (see e.g. the mass balance).

The basic idea of FEM is the consideration of the so-called spatial *weak formulation* of the above PDE using a sufficiently smooth[9] test function $\eta(\underline{x}) \in \mathbb{H}^1$. This function must vanish at the

---

[8] The plastic strains $\underline{\underline{\varepsilon}}^{\mathrm{pl}}(n-1)$ vanish, if elastic material behaviour occurred during the time step $(n-1)$.
[9] In the mathematical sense this condition ensures differentiability. The set of all suitable functions is denoted by $\mathbb{H}^1$, the so-called HILBERT space or the space of square-integrable functions.

boundary, $\partial\Omega$, of the domain, $\Omega$, of the body, i.e., $\eta = 0$ for all $\underline{\mathbf{x}} \in \partial\Omega$ (the so-called zero conditon). Multiplying Eq. (15) with $\eta$ and subsequent integration on $\Omega = \{\underline{\mathbf{x}}|\underline{\mathbf{x}} \in \mathbb{R}^3\}$ yields:

$$\int_\Omega R\eta \, \mathrm{d}\underline{\mathbf{x}} = 0 \, . \tag{16}$$

Thus, the quantity $w$ must be chosen such, that the integral (or functional) of Eq. (16) becomes minimal (i.e., zero). This task is typical for so-called variation problems, in which extrema of 'functions of functions' are calculated. The variable $R$ is often called the residuum and represents the deviation from the 'correct solution'.

For the most engineering problems the formulations of Eq. (15/16) are equivalent. The advantage of Eq. (16) follows by partial integration, viz.

$$\int_\Omega \left[\eta\partial_t w + \underline{\boldsymbol{\nabla}}\eta \cdot \tilde{\underline{\mathbf{f}}}(w) - s\eta\right] \mathrm{d}\underline{\mathbf{x}} = 0 \, . \tag{17}$$

in which the boundary terms vanish due to the above mentioned zero-condition. Two items are obvious in Eq. (17): **(a)** the order of derivation of $w$ w.r.t. $\underline{\mathbf{x}}$ has reduced and **(b)** the derivation changed to the test function.

So the required order of differentiability for the function $w$ has reduced by one. Therefore the solution of Eq. (17) for arbitrary test functions $\eta$ is called the weak solution of the origin PDE.

The unknown field quantity $w$, the test function, and all required derivatives of these quantities can be decomposed into contributions of the $n$ elements following from the discretization of the system. By means of weighted basis functions (also denoted as ansatz functions) the following approximation is derived (GALERKIN method):

$$w(\underline{\mathbf{x}}) = \sum_i^n \alpha_i N_i(\underline{\mathbf{x}}) \quad , \quad \underline{\mathbf{w}}'(\underline{\mathbf{x}}) = \sum_i^n \alpha_i \underline{\mathbf{N}}_i'(\underline{\mathbf{x}}) \, , \tag{18}$$

$$\eta(\underline{\mathbf{x}}) = \sum_i^n \beta_i N_i(\underline{\mathbf{x}}) \quad , \quad \underline{\boldsymbol{\eta}}'(\underline{\mathbf{x}}) = \sum_i^n \beta_i \underline{\mathbf{N}}_i'(\underline{\mathbf{x}}) \, , \tag{19}$$

with the unknown coefficients $\alpha_i$ (also denoted as node variables), the arbitrary factors $\beta_i$ and the ansatz functions $N_i$. Usually the ansatz functions are approximated by power series of first, second or higher order, which - consequently - lead to the notation of linear, square, or higher order elements. Note that the computational effort considerably increases with rising order, since the number of nodes required for the calculation of the ansatz functions increases, namely n+1 (linear), 2n+1 (square), etc..

Inserting Eq. (18, 19) into Eq. (17) yields the following expression:

$$\sum_j \beta_j \left[\frac{\mathrm{d}}{\mathrm{d}t}\sum_i \alpha_i \int N_i N_j \, \mathrm{d}\underline{\mathbf{x}} + \sum_i \alpha_i \int \tilde{\underline{\mathbf{f}}}(N_i, \underline{\mathbf{N}}_i', \ldots) \cdot \underline{\mathbf{N}}_j' \, \mathrm{d}\underline{\mathbf{x}} - \int s N_j \, \mathrm{d}\underline{\mathbf{x}}\right] = 0 \tag{20}$$

or - by successive consideration of $(\beta_1 = 1, \beta_2 = 0, \ldots, \beta_n = 0)$; $(\beta_1 = 0, \beta_2 = 1, \ldots, \beta_n = 0)$; etc. - an Ordinary Differential Equation (ODE) system of dimension $n$:

$$\frac{\mathrm{d}}{\mathrm{d}t}\left[\underline{\underline{\mathbf{M}}} \cdot \underline{\boldsymbol{\alpha}}\right] + \underline{\underline{\mathbf{K}}} \cdot \underline{\boldsymbol{\alpha}} - \underline{\mathbf{s}} = 0 \, , \tag{21}$$

Modeling, Simulation and Experimental Studies of Distortions,
Residual Stresses and Hydrogen Diffusion During Laser Welding of As-Rolled Steels

83

which, in turn, can be solved by forward/backward time integration methods (e.g. EULER prodedure). Finally it is worth-mentioning that the calculation of $\underline{\mathbf{M}}$, $\underline{\mathbf{K}}$ (the so-called mass and stiffness matrix) and $\underline{\mathbf{s}}$ requires a numerical integration. For this reason the integrals are replaced by weighted sums as follows:

$$\int N_i(\underline{\mathbf{x}})\,\mathrm{d}\underline{\mathbf{x}} \cong \sum_{p=1}^{n_p} N_i(\underline{\mathbf{x}}_p) W_p \,. \tag{22}$$

Here the functions $N_i$ are only calculated at representative points (the so-called GAUSS points[10]) by using the weight factors $W_p$. Position and typical number of the points $\underline{\mathbf{x}}_p$ as well as the according weight factors can be found in the literature, e.g. (Wriggers, 2000).

### 2.4 An example for the FEM formalism - heat transfer equation

In order to illustrate the above, slightly abtract, explanations the corresponding equations will be derived for the heat transfer problem within this paragraph. For this purpose the balance of internal energy in Eq. (3) including FOURIER's law of heat conduction in Eq. (4) and the caloric equation of state in Eq. (5) is considered and terms of velocity gradients (dissipation) are neglected. The resulting equation is known as the instationary heat transfer equation and reads:

$$\rho c_{\mathrm{P}} \frac{\mathrm{d}T}{\mathrm{d}t} - \underline{\boldsymbol{\nabla}} \cdot \underline{\underline{\boldsymbol{\kappa}}} \cdot \underline{\boldsymbol{\nabla}}T = r \quad \text{with} \quad \mathrm{d}_t(\cdot) = \partial_t(\cdot) + \underline{\mathbf{v}} \cdot \underline{\boldsymbol{\nabla}}(\cdot) \,. \tag{23}$$

The weak formulation follows by applying the product rule and the divergence theorem analogously to Eq. (17):

$$\int_{\Omega} \rho c_{\mathrm{P}}(\mathrm{d}_t T)\eta\,\mathrm{d}\underline{\mathbf{x}} + \int_{\Omega} \underline{\underline{\boldsymbol{\kappa}}} \cdot \underline{\boldsymbol{\nabla}}T \cdot \underline{\boldsymbol{\nabla}}\eta\,\mathrm{d}\underline{\mathbf{x}} = \int_{\partial\Omega} \underbrace{(\underline{\underline{\boldsymbol{\kappa}}} \cdot \underline{\boldsymbol{\nabla}}T)}_{=\underline{\mathbf{q}}_n}\eta \cdot \underline{\mathbf{n}}\,\mathrm{d}A + \int_{\Omega} r\eta\,\mathrm{d}\underline{\mathbf{x}} \,. \tag{24}$$

Here the symbol $\underline{\mathbf{q}}_n$ represents the heat flux through the surface of the volume and is usually replaced by the ansatz $\underline{\mathbf{q}}_n = \alpha(T - T_0) \cdot \underline{\mathbf{n}}$, ($\alpha$: heat transfer coefficient and $T_0$: surrounding temperature). By performing afore mentioned procedure of discretization one finally finds, cp. also (Kang & Im, 2007):

$$\underline{\underline{\mathbf{M}}} \cdot \frac{\mathrm{d}\underline{\mathbf{T}}}{\mathrm{d}t} + \underline{\underline{\mathbf{K}}} \cdot \underline{\mathbf{T}} = \underline{\mathbf{Q}} + \underline{\mathbf{R}} \,, \tag{25}$$

the following components of matrices and vectors ($i, j = 1, \ldots, n$):

$$M_{ij} = \int_{\Omega} \rho c_{\mathrm{P}} N_i N_j\,\mathrm{d}\underline{\mathbf{x}} \quad , \quad K_{ij} = \int_{\Omega} \underline{\underline{\boldsymbol{\kappa}}} \cdot \underline{\mathbf{N}}_i' \cdot \underline{\mathbf{N}}_j'\,\mathrm{d}\underline{\mathbf{x}} \,, \tag{26}$$

$$Q_i = \int_{\partial\Omega} \alpha N_i (T - T_0)\underline{\mathbf{n}} \cdot \underline{\mathbf{n}}\,\mathrm{d}A \quad , \quad R_i = \int_{\Omega} r N_i\,\mathrm{d}\underline{\mathbf{x}} \,. \tag{27}$$

in which $\underline{\mathbf{T}} = (T_1, \ldots, T_n)$ stands for the vector including the unknown temperatures of the single elements. The ODE system of Eq. (25) can be numerically solved for appropriate initial conditions.

---

[10] The underlying method of numerical integration is often called the GAUSS integration or GAUSS quadrature.

**2.5 Geometry, meshing, heat sources, boundary and initial conditions for laser welding**

First, the question arises: What means 'simulation of welding'? Basically, this means the calculation of materials response - howsoever - after moving a heat source over two kinds of metals, which are (initially) separated and jointed after the heat supply. This response can be manifold depending on focus and complexity of modelling, e.g.:

- The development of a spatially and temporally changing temperature field including melting zone (welding pool), fluid dynamics (MARAGONI effect) and solidification.

- Thermal expansion, distortion, and the formation of residual stresses within the material during and after the joining process.

- Phase transformation and TRIP (Transformation Induced Plasticity) effects.

- Hydrogen diffusion (activation of trapped hydrogen, increasing hydrogen in regions of high tensile stresses due to diffusion).

- Material income due to filler metals.

- Changes of the geometry, e.g. seam bulging or gap closing.

Obviously, the material response is notedly complex and, therefore, only aspects are considered. Consequently, it is essential to, firstly, clarify the demands on the simulation and the leading effects, which should be modelled.

Starting point of each welding simulation is the (spatially changing) heat input, which is - in case of laser welding - extremely local (in magnitude of the laser diameter, $d = 0.5\ldots1.5$ mm). Due to the high power of the laser-beam ($P_{laser} = 38$ KW), considerable temperatures accompanying with high temperature gradients and heat fluxes are usually observed. In contrast, several millimetres adjacent to the seam the temperature is already moderate and partially even below $100\,°C$. Therefore a spatial discretization (mesh) must be chosen, which is extremely fine in the vicinity of the seam and which coarsens for distant regions. Moreover, to save computational times we restrict the consideration to a Representative Sheet Element (RSE), instead of the complete coil/strip-width ($b_c \approx 800\ldots1650$ mm). This restriction only holds, if boundary effects in the middle of the $x$- and $y$-direction of the RSE can be neglected or - with other words - if the calculated fields (mass density, temperature and displacements) are geometrically similar for the RSE and the real coil geometry. Figure 5 (left) shows the explained strip, the RSE and the chosen measures for the simulation. Figure 5 (right) illustrates the global FE mesh of the considered RSE together with two detailed views. As one can see, the mesh is much finer in the vicinity of the welding seam. The gap between both sheets is chosen as $s = 0.2$ mm, and the effect of bulging and gap closing is realized by the `Ekill-Ealive` technique provided by the ANSYS® program package. For this purpose the gap as well as the bulging elements are a priori modeled and meshed. Subsequently these elements are deactivated, which means that its contributions within the mass and stiffness matrix are multiplied with a 'numerical zero' (e.g. $10^{-6}$). Thus the elements do not contribute to the solution during simulation. Deactivated elements, for which the moving heat source has passed and which fall below the melting temperature, are successively activated, i.e., the above mentioned artificial multiplication is canceled. Hence the corresponding elements contribute to the solution in the proceeding simulation (Ansys theory ref., 2007). This procedure allows to model materials input as well as joining.

The translation of the heat source is defined by the process parameter of welding velocity and direction, whereas the characteristics of heat input (heat source dimension, power
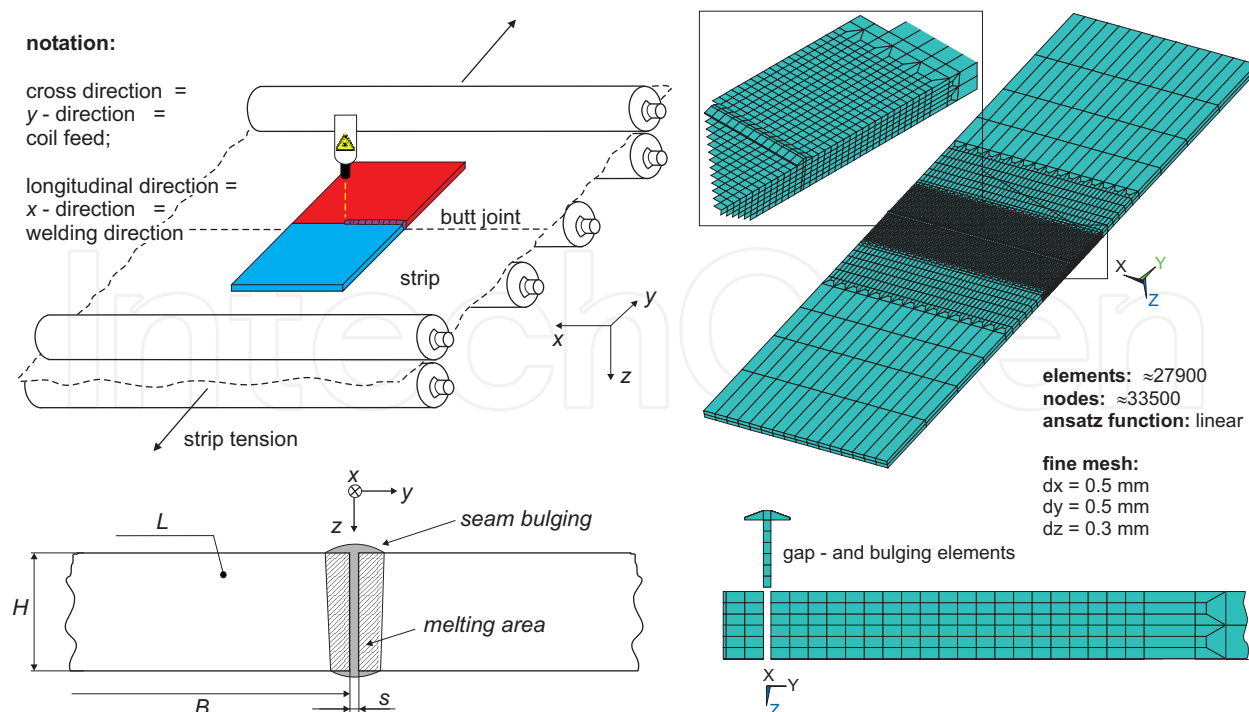
Fig. 5. *Left*: Illustration of the RSE and the chosen geometry data of the RSE: $H = 1.8$ mm, $L = 50$ mm, $B = 75$ mm, $s = 0.2$ mm. *Right*: Illustration of the simulation geometry and the used FE discretization including various meshing data.

distribution, total heat, supply over surface or keyhole) is determined by the method of welding (laser, MIG/MAG, TIG, etc.) and the welding power.

The manner of supplying the heat into the metal as well as the resulting melt pool directly determines the developing temperature distribution. Consequently the realistic modeling of the heat supply is a crucial task of welding simulations. The best strategy in this context would be a coupled consideration of **(a)** the melting process due to heat input, **(b)** the laser-welding-specific vaporization process leading to a vapor capillary in the melt, in which the laser beam can repeatedly be reflected, which - in turn - allows for a deep heat input, and **(c)** the melt pool dynamics, which affects the geometry and dimension of the melting area.

However a complete numerical analysis of the multiphase fluid dynamics problem with subsequent simulation of the solid material w.r.t. resulting temperatures, stresses and microstructure (phases, grains, etc.) is an ongoing challenge. Therefore the literature[11] mainly contains two kinds of investigations:

**(1)** Considerations of fluid dynamics aspects: This item incorporates e.g. modeling of drop formation and impingement during TIG or MIG/MAG welding (Fan & Kovacevic, 1999; Zhou & Tsai, 2008); investigations of the influence of different chemical elements (such as S) on melt flow and the weld pool geometry (Lee et al., 1998; Mills et al., 1998; Wang et al., 2001; Wang & Tsai, 2001); simulation of the keyhole dynamics during laser welding (Ki et al., 2002; 2002a; Pfeiffer & Schulz, 2009); or the analysis of asymmetric melt pool geometries due to dissimilar materials (Phanikumar et al., 2004). Consequences on residual stresses, distortions or microstructure in the solid state are not - as far as known - considered.

---

[11] The chosen literature references are not complete; they are examples of the recent years.

**(2)** Solid-state calculations, which assume an ad-hoc or experimentally verified melt pool geometry: Thus, a temperature or power distribution is *a priori* defined at the melt pool or at the region of heat input. Then the resulting global temperature distribution, stresses, distortions, or microstructures can be calculated (Dean et al., 2003; Hemmer & Grong, 1999; Hemmer et al., 2000; Spina et al., 2007). Moreover, also complex geometries (Tian et al., 2008), multi-pass welding (Dean et al., 2008; Dean & Hidekazu, 2008), cracking caused by shrinkage (Dong & Wei, 2006), or the process-chain bending-welding (Khiabani & Sadrnejad, 2009) have been simulated with sufficient accuracy.

In the following the strategy of the second item is employed[12]. To this end the ANSYS® specific program library LASIM is used, (Junk & Groth, 2004). Here the geometry parameter $x_{r/f}^{1/2/3}$, $y^{1/2/3}$, and $z^{2/3}$ as well as the total power input must by defined, cf. Figure 6. The (parabolic) power distribution is applied to the nodes of the three illustrated planes such, that the sum reproduces the total power. Alternatively, various authors use a GAUSSian
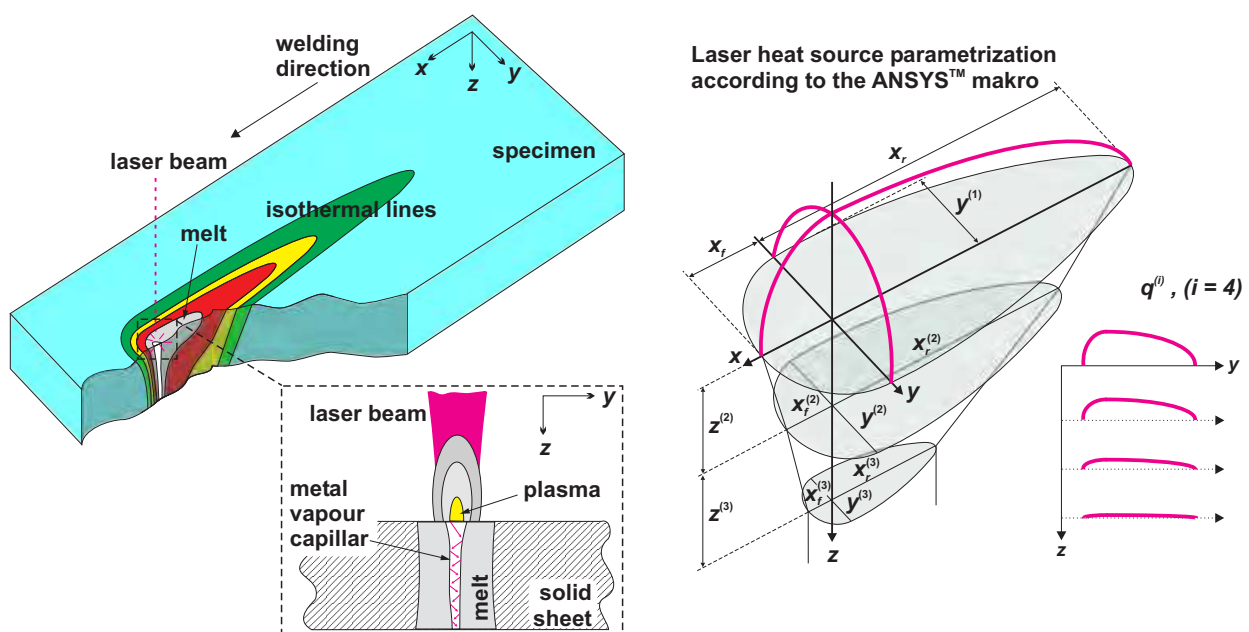


Fig. 6. Melt pool geometry during laser welding and the laser specific LASIM distribution.

distribution, according to the cross-sectional power distribution of the laser beam, e.g. (De et al., 2003), see also Figure 7, to model the welding heat source. It reads:

$$q(x,y,i) = Q(i)\frac{1}{2\pi\sigma^2}\exp\left[-\frac{x^2+y^2}{2\sigma^2}\right].$$ (28)

The variables $x$ and $y$ represent the components of the distance vector between the center of the laser beam and a point of the planar environment. The value of $\sigma$ stands for the standard deviation of the normal distribution $q/Q_i$ and characterizes the variance of the distribution. The variable $i$ identifies the different planes and allows for a volumetric heat input (depth effect) due to melt pool dynamics. In particular holds for $Q(i)$ in Eq. (28):

$$Q(i) = Qf_i \quad \text{and} \quad \sum_i f_i = 1.$$ (29)

---

[12] There are also attempts to couple fluid dynamics and solid state calculations (see also the Discussion at the end of the work).

A typical choice, for example, can be: $i = 3$, $f_1 = 0.75$, $f_2 = 0.2$, $f_3 = 0.05$, so that the first three planes of the $z$-directions are used for heat input. Furthermore it is worth mentioning,
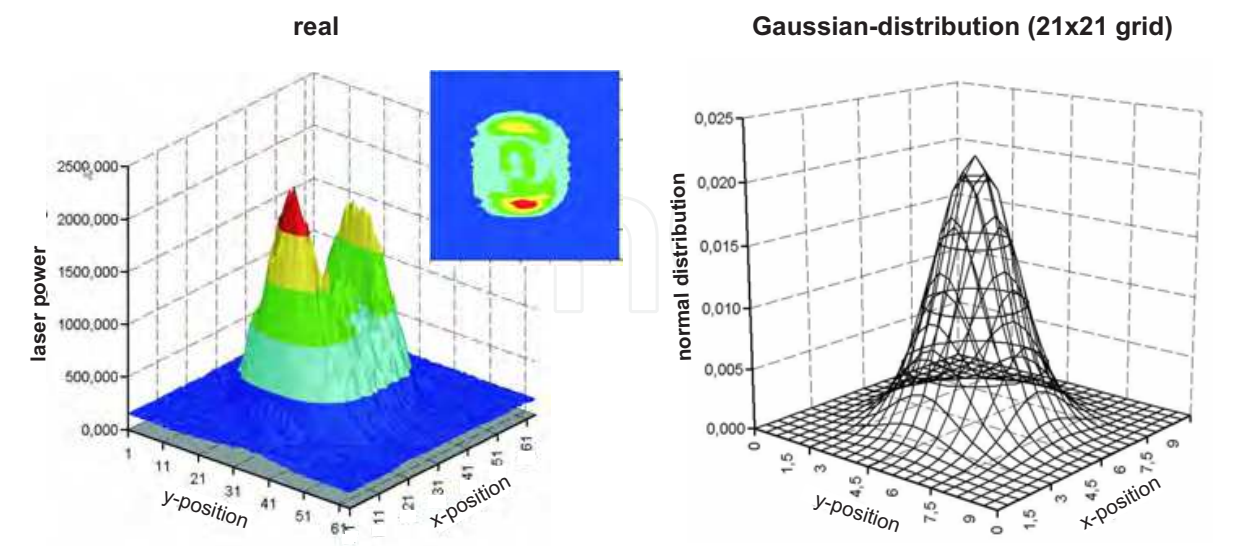
**real**                           **Gaussian-distribution (21x21 grid)**



Fig. 7. Cross sectional power distribution of the laser beam: real case (*left*) and modeling case (*right*, GAUSSian distribution).

that the real heat absorption into the sheets considerably differs to the value adjusted at the laser beam source. The majority of power is reflected, passes the material, or dissipates by heating the environment. The remaining power consumed by welding can be described by means of the efficiency $\eta$:

$$Q = \eta\, P_0 \quad , \quad (P_0: \text{origin power of the laser source}) . \tag{30}$$

The efficiency $\eta$ depends on the material thickness $d$, the gap width $s$, the welding velocity $v_s$, or the laser type (e.g. $CO_2$- or solid-state-laser). In the present case, i.e., for butt welding with $CO_2$-laser, experiments show the following empiric relation, (Kotowski, 1998):

$$\eta_{CO2} = 0.0053\, s\, v_s + 3.3854\, d\, v_s + 9.2073\, d + 0.0581\, s + 1.1094\, v_s + 0.1866 \tag{31}$$

with $d$ in [mm], $s$ in [mm] und $v_s$ in [m/min]. Consequently an efficiency of $\eta = 0.43$ is derived for $s = 0.2$ mm and $v_s = 5$ m/min.

In order to numerically solve the required balance equations, thermal and mechanical boundary conditions must be specified. So, the strip is clamped by copper shoes few millimetres adjacent to the seam $(3 \ldots 3.5 \text{ mm})$ from the upper and lower side, cf. Figure 8 (magenta region). The upper side of the strip is exposed to an inert gas (Helium) flow in the vicinity of the seam; thus *forced convection* takes place. Furthermore the lower side of the strip is in *thermal contact* with another steel surface, which leads to heat transfer and to enhanced cooling of the strip. The remaining (free) surfaces of the strip (RSE), e.g. the lower side of the joining area, release heat by *radiation and free convection*, cf. Figure 8. All kinds of heat transfer over the surfaces can be described by means of (different) heat transfer coefficients, $\alpha$. The corresponding equations and values are summarized in the **Appendix** at the end of this work. Please also note, that the welded parts of the butt joint can conduct heat, and the corresponding surfaces cannot independently move (in contrast to the origin state), since they are mechanically jointed, cf. Figure 8. Finally, initial conditions have to be specified, from which the time integration starts; here we used: $T(\underline{\mathbf{x}}, t = 0) = T_0$ and $\underline{\mathbf{u}}(\underline{\mathbf{x}}, t = 0) = \underline{\mathbf{0}}$.
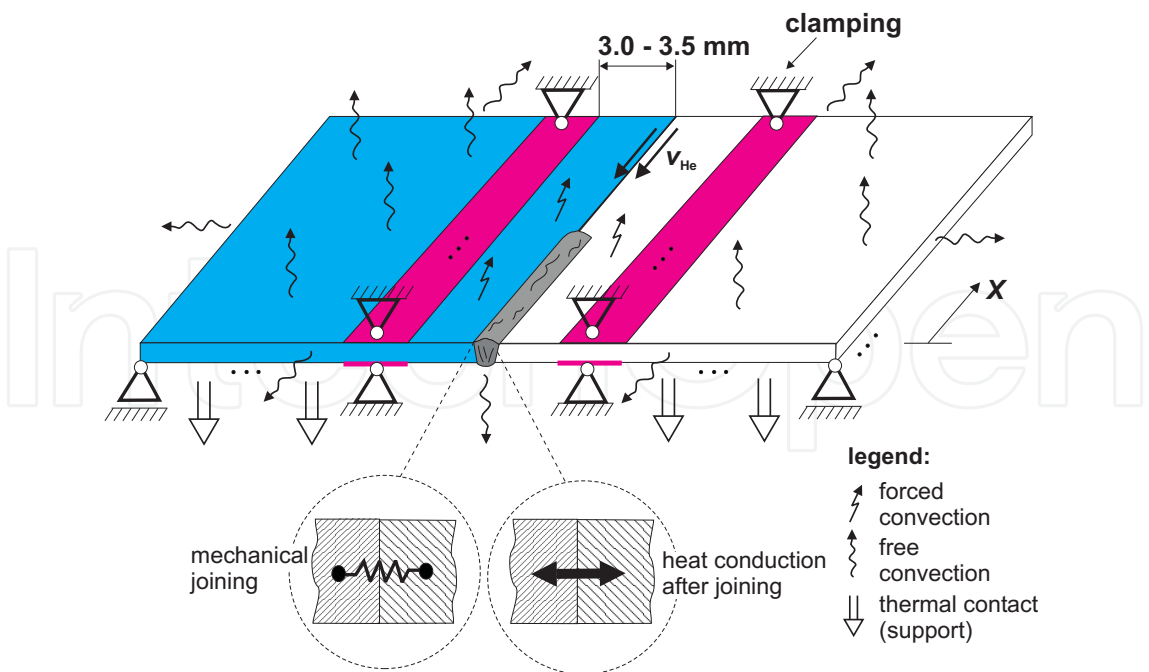
Fig. 8. Illustration of the used boundary conditions due to the conditions of the manufacturing line.

## 3. Materials data

The following considerations exclusively refer to the investigated TRIP 700 steel; the composition is depicted in Table 1.

|        | C    | Al   | Mn   | Si   | P    | B     | Cr+Mo | Nb+Ti |
|--------|------|------|------|------|------|-------|-------|-------|
| **max.** | 0.24 | 1.60 | 2.00 | 0.30 | 0.04 | 0.005 | 0.60  | 0.20  |

Table 1. Composition of the investigated TRIP 700 steel.

### 3.1 Caloric data

To solve the heat conduction equation the following temperature-depending materials data are required additionally to the data accomplished in the **Appendix**: heat conductivity (here for the isotropic case: $\underline{\underline{\kappa}} = \kappa \underline{\underline{I}}$), mass density $\rho$, and specific heat capacity $c_{\mathrm{p}}$ (or enthalpy density $h$ instead of $\rho$ and $c_{\mathrm{p}}$). These quantities are determined - in a first approximation - by means of the assumption[13] of infinitely slow heating and quenching. Figure 9 (left) shows the different equilibrium phases, which constitute at various temperatures. The right picture of Figure 9 illustrates the transition between solid and liquid phase in the vicinity of the melting point ($T_{\mathrm{solidus}} = 1457\,^{\circ}\mathrm{C}$ and $T_{\mathrm{liquidus}} = 1457\,^{\circ}\mathrm{C}$). The thermal materials data used (later) in the simulations are illustrated in Figure 10. For comparison experimental values, which were

---

[13] This assumption leads to constant transformation temperatures. Any shifts of the phase transformations due to varying heating/quenching rates $\dot{T}$ are excluded. For the consideration of materials data depending on $T$ and $\dot{T}$ transformation models must be applied, (Avrami, 1939; 1940; Koistinen & Marburger, 1959; Leblond & Devaux, 1984). Such models take the temperature history into account and allow for the calculation of e.g. different phase volume fractions and the resulting materials data, (Kang & Im, 2007).
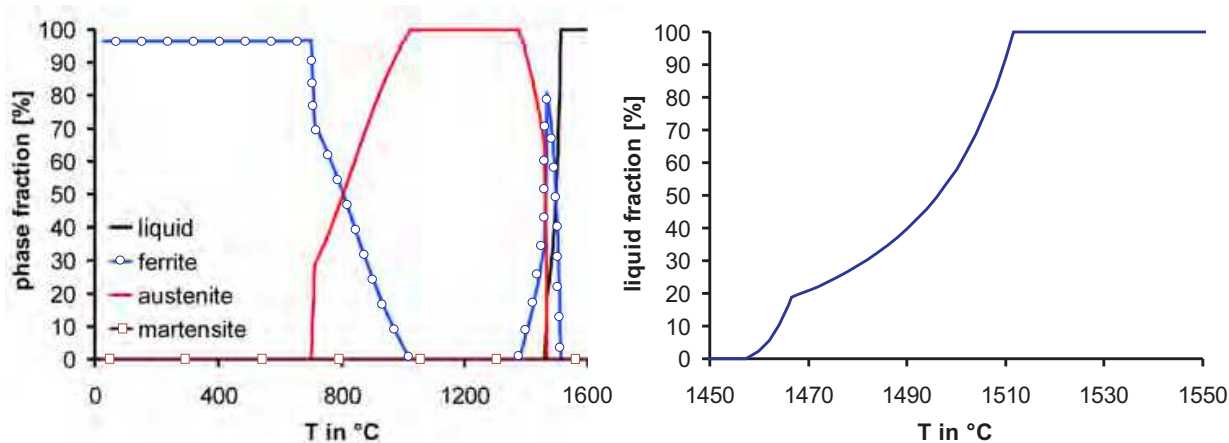
Modeling, Simulation and Experimental Studies of Distortions,
Residual Stresses and Hydrogen Diffusion During Laser Welding of As-Rolled Steels

89

Fig. 9. Different equilibrium phases in TRIP 700, calculated with JMATPRO, (JMatPro, 2011).

found in literature[14], (Barth & Groß, 2004), are also displayed. Finally it is worth mentioning, that the conductivity is artificially multiplied by the factor 3 for temperatures $T > \frac{1}{2}(T_{\text{solidus}} + T_{\text{liquidus}})$. Thus the effect of enhanced conductivity due to melt pool dynamics is taken into account.
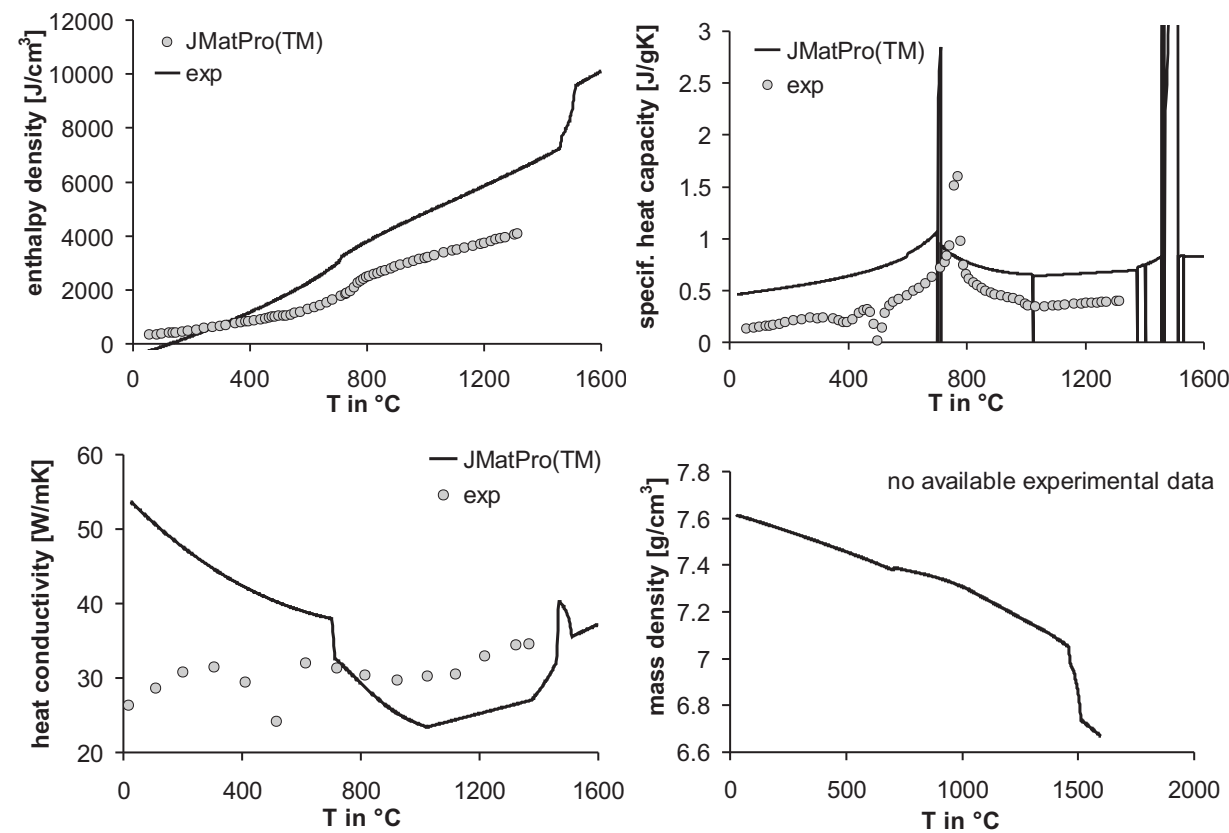


Fig. 10. Calculated and experimental, thermodynamic materials data as functions of the temperature.

---

[14] The conductivity is indirectly measured by using the temperature conductivity $a$ and the relation $\kappa = \rho\, c_{\text{p}}\, a$.

### 3.2 Experimental determination of mechanical materials data

Beyond the caloric data, the solution of the balance of momentum requires temperature-depending data for YOUNG's modulus , POISSON ratio (for HOOKE's law), and the work-hardening behavior of the material. In commercial FE-program packages, such as ANSYS®, the work-hardening characteristic of the material is defined via data-sets, representing the (1D-)yielding curve at different temperatures. For values between or beyond the temperatures used for the definition of the curves an interpolation is performed or the curve of the highest temperature is applied.

Mechanical data for as-rolled steels are rarely available and, therefore, experiments must be performed. For this reason tensile tests, realized at the Gleeble 3500®, are analyzed for the temperatures 20 °C, 100 °C, 300 °C, 600 °C, 1100 °C and 1200 °C, cf. Figure 11. Here specimen heating follows from the electrical resistance and JOULE's (heat) effect, viz:

$$\mathrm{d}W_{\mathrm{Joule}} = U\,I\,\mathrm{d}t \qquad , \qquad (\text{JOULE's effect}) \,, \tag{32}$$

$$I = \frac{A\,U}{\rho_{\mathrm{R}}(T)\,l} \qquad , \qquad (\text{conductor with cross-area } A, \text{ length } l) \,, \tag{33}$$

$$\rho_{\mathrm{R}}(T) \approx \rho_0 \frac{T}{T_0} \qquad , \qquad (\text{specific resistance}) \,, \tag{34}$$

with $\rho_0 = 0.1\ldots 0.2 \cdot 10^{-6}$ Ωm.

It should be pointed out, that the specimen is cooled in the boundary region due to the (cold) clampings; consequently a temperature gradient is formed in loading direction. To minimize temperature gradients within the measured distance a reduced reference length of $L_0 = 25$ mm is used, contrary to the DIN EN 100002-1, (DIN, 2001). The temperature control is carried out via a Thermo-Couple-Element (TCE) at the middle of the specimen-length and -width. The temperatures used for tensile tests are chosen such, that no phase transformation occurs during testing. For this reason, first, the (unloaded) specimen is slowly heated to determine the transformation temperatures. Figure 12 displays the heating procedure (upper left) as well as the resulting width variation of the specimen (upper right). Here the 'jumps' represent the phase transformations, for which the following temperatures hold: The change of width

*Ac1* ≈ *770 °C (start of austenite formation)* ,      *Ar1* ≈ *600 °C (start of ferrite formation),*
*Ac3* ≈ *940 °C (total austenite)* ,                          *Ar3* ≈ *520 °C (total ferrite).*

for different temperatures, cf. Figure 12 (upper right), can be directly used to calculate the averaged thermal expansion coefficient via the relation: $\alpha = \Delta b / [b_0(T - T_0)]$, cf. Figure 12 (lower right). Here only the heating procedure is exploited and - according to the high temperature behaviour of steel, c.f., (Richter, 1973) - a linear extrapolation up to the melting point is performed.

The stress-strain curves measured at different temperatures are illustrated in Figure 13. For each temperature two tensile measurements were exploited to obtain the temperature-depending 1D-stress-strain response of the material. However, the pictures exemplarily display one curve and the averaged discrete values (dots) used - together with YOUNG's modulus, cf. Figure 15 (right) - to construct the final curves for simulation, cf. Figure 13 (lower right). Figure 14 explains the strategy of the tensile tests exemplarily for

two temperatures. The specimen is firstly heated (cp. Figure 12, lower right) such, that any displacements are permitted to avoid any internal stresses due to thermal expansion. After reaching the target temperature the specimen is strained up to failure by controlling the displacements. For heating as well as straining moderate rates, i.e., $dT/dt = 3$ K/s and $dl/dt = 20$ μm/s, are used. Thus, the assumption of phase equilibrium holds at all times, and any viscose effects are minimized.

In order to determine the temperature-depending YOUNG's modules, $E$, an additional test was performed. Due to clamping relaxations and insufficient measuring deviations the consideration of the primary loading curve for $E$ is questionable. This flaw is also mentioned within the DIN EN 100002, (DIN, 2001), and, therefore the authors recommend the determination of $E$ by using the unloading regime. Here the point of unloading must be chosen beyond yielding but 'appreciable' before necking. In the present investigations two unloading procedures are performed for each tensile test, in which the averaged slope represents YOUNG's modulus. Here the curves in Figure 13 can be exploited to define appropriate stresses for 'inserting' the unloading procedure. The subsequent, separate test is arranged such, that the specimen are stressed (force-controlled) up to the predefined starting points for unloading and, then, unloaded up to 1/10 of the applied maximal stress. After
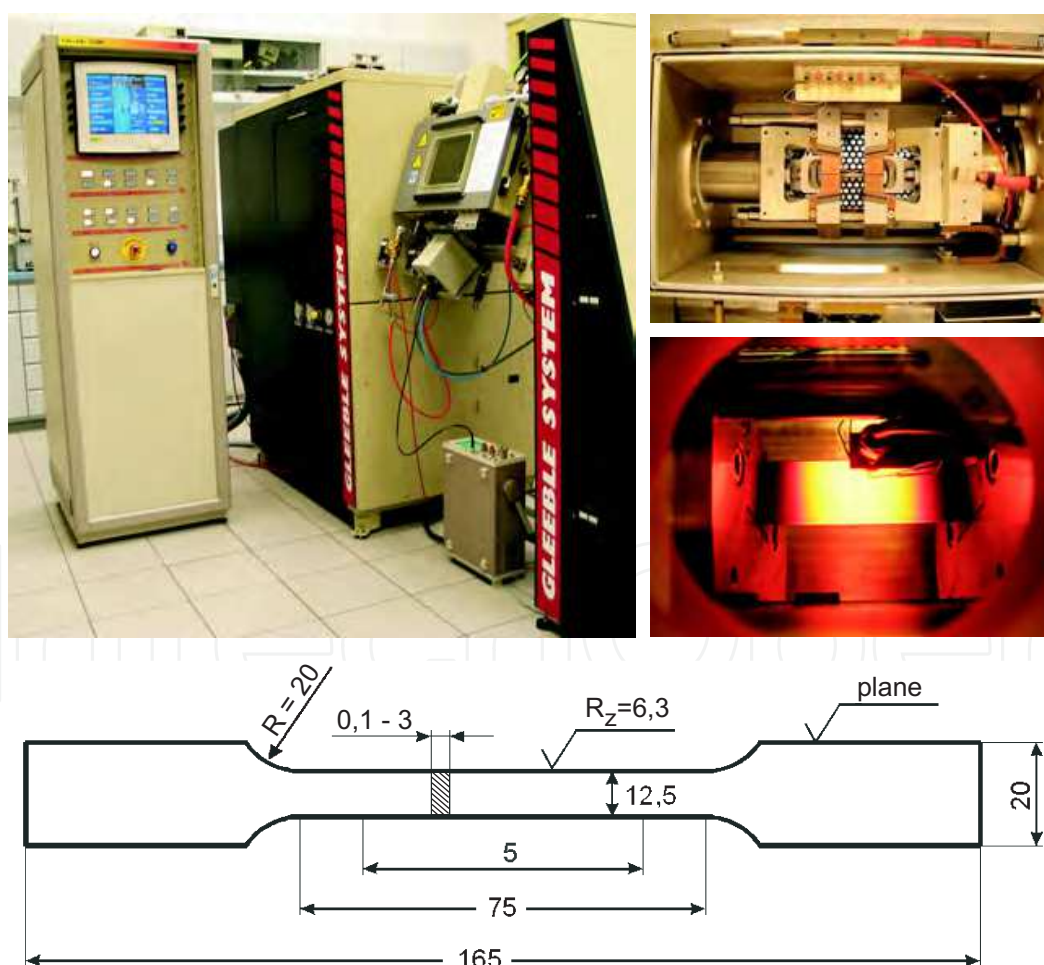


Fig. 11. Gleeble3500® used for the temperature-depending tensile test and geometry of the specimen.
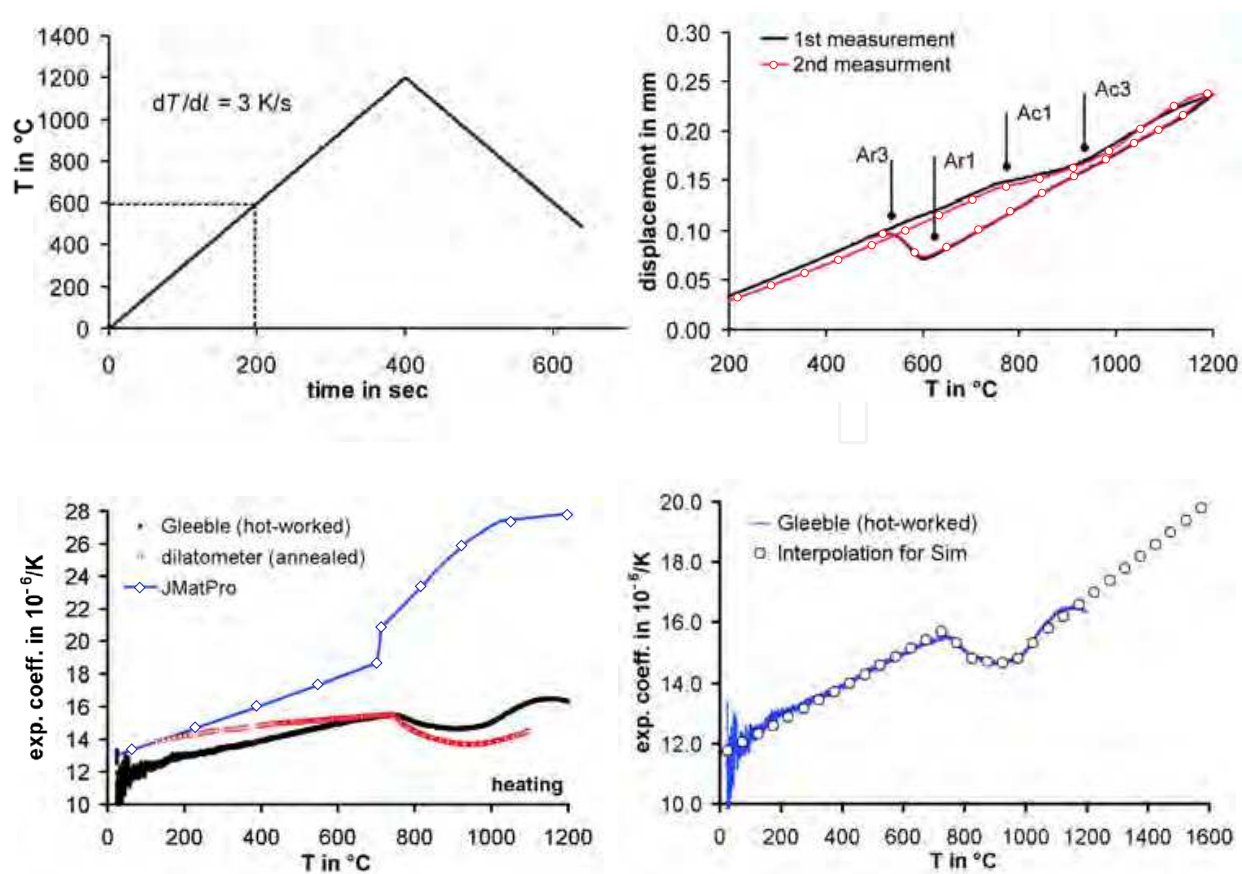
Fig. 12. *First row*: Determination of regions of transformation. *Second row*: Experimentally fitted thermal expansion coefficients (including the comparison with data of annealed material and JMATPRO).

the second unloading the test is finished by fast loading up to failure, cf. Figure 15 (left). The resulting cyclic curves are illustrated in Figure 16 for the temperatures $T = 20$ °C and 100 °C. The right pictures demonstrate the determination of $E$ by averaging the slope of the two unloading regimes. In summary, the values of Table 2 were found, which are displayed in Figure 15 (right). Note, that the fitted function has not physical meaning. It simply reproduces the experimental values and the side condition: $E > 0$ for $T \rightarrow \infty$. In many cases,

| $T$ [°C] | 20 | 100 | 300 | 600 | 1100 | 1200 |
|---|---|---|---|---|---|---|
| $E$ [GPa] | 246.0 | 177.6 | 164.8 | 139.0 | 103.1 | 83.7 |

Table 2. YOUNG's modulus for different temperatures obtained from experiments (TRIP 700, as-rolled).

alternatively to experimentally obtained stress-strain curves, temperature-depending discrete values for $E$, $R_{p02}$, $R_m$ and $A_g$ (uniform strain) are available. Then an optimization procedure can be performed by using, for instance, a RAMBERG-OSGOOD power law as follow:

$$\varepsilon = \varepsilon^{\text{elast}} + \varepsilon^{\text{plast}} = \frac{\sigma}{E} + \left(\frac{\sigma}{K}\right)^{1/n} \ . \tag{35}$$
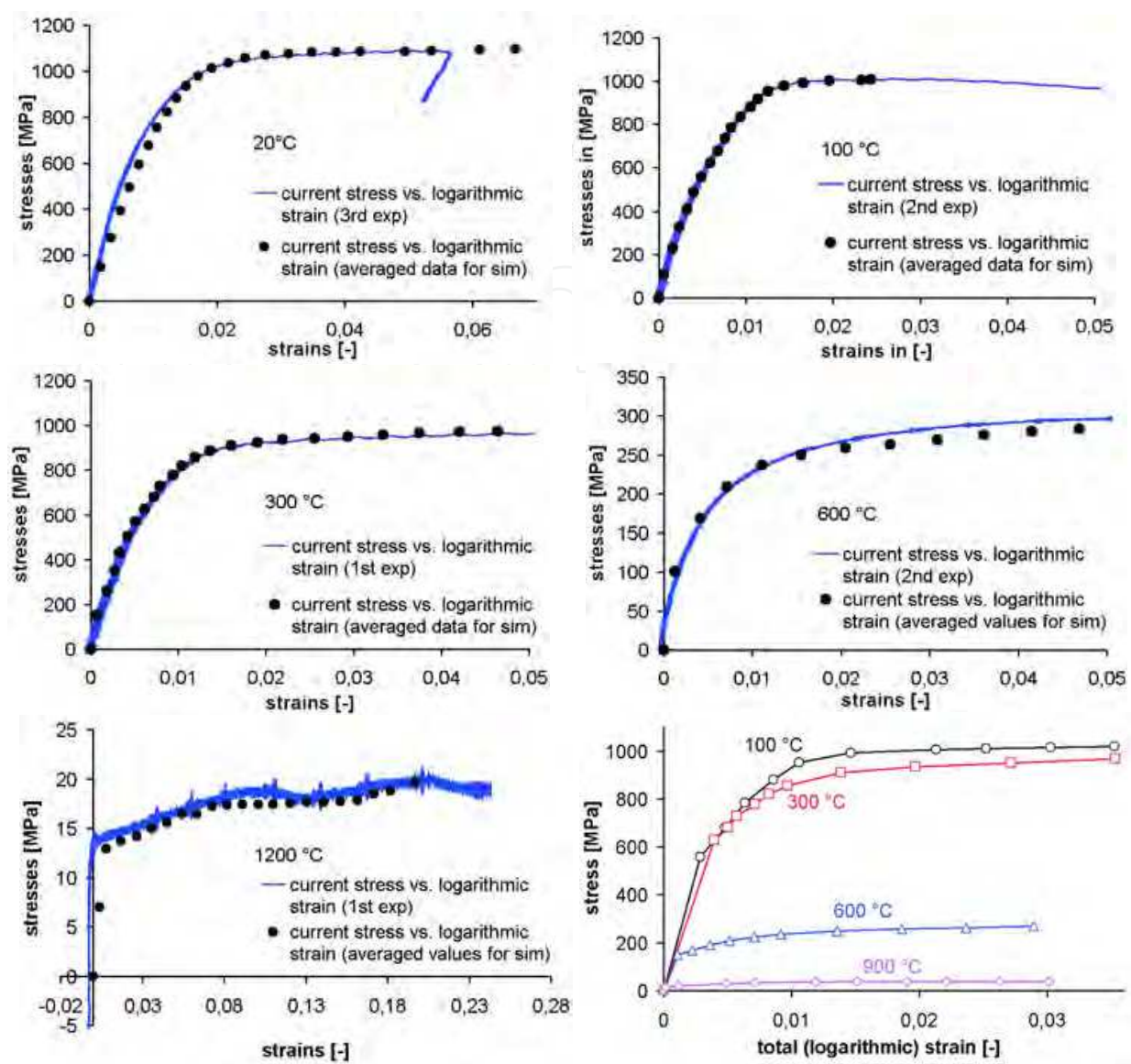
Fig. 13. Measured stress-strain curves for various temperatures including the implemented curves used in the ANSYS® simulation (exemplarily, lower right).

The two arbitrary parameters $K$ and $n$ must be optimized such, that the deviation between the resulting function and the experimental values:

$$\varepsilon^{(1)} = 0.002 + \frac{R_{p02}}{E} \qquad , \qquad \varepsilon^{(2)} = A_g + \frac{R_m}{E} \tag{36}$$

are sufficiently minimal. For this reason the root-mean-square deviation:

$$\sum_{i=1}^{2} \left[ \varepsilon^{(i)} - \frac{\sigma}{E} - \left( \frac{\sigma}{K} \right)^{1/n} \right]^2 \longrightarrow \min \tag{37}$$

can be considered. The minimum of Eq. (37) results e.g. by using a gradient-based algorithm, which is typically available in commercial program packages, such as Matlab® (Mathworks Inc.) or Excel (Microsoft® Corp.). Figure 17 shows the result of the explained procedure using
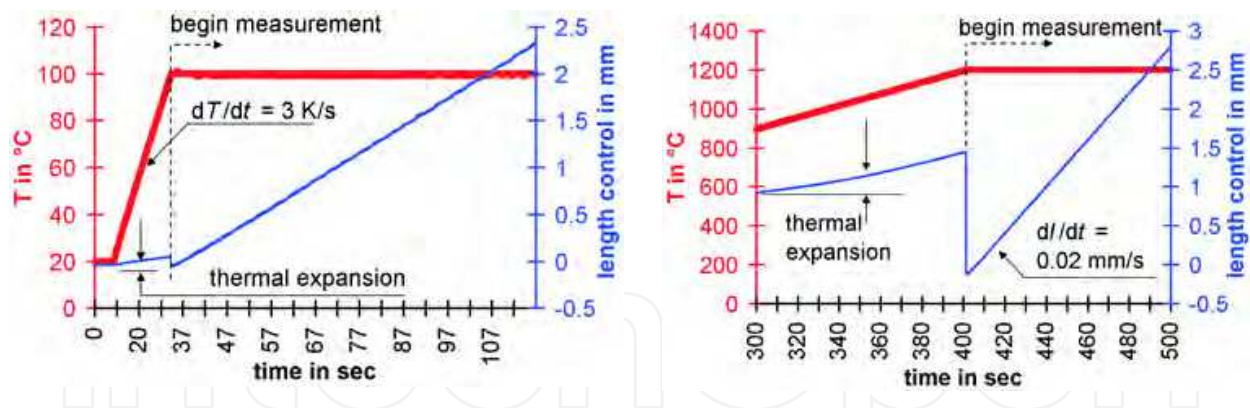
Fig. 14. Heat and loading procedure for two, exemplary, tensile tests (T = 100 °C and 1200 °C).
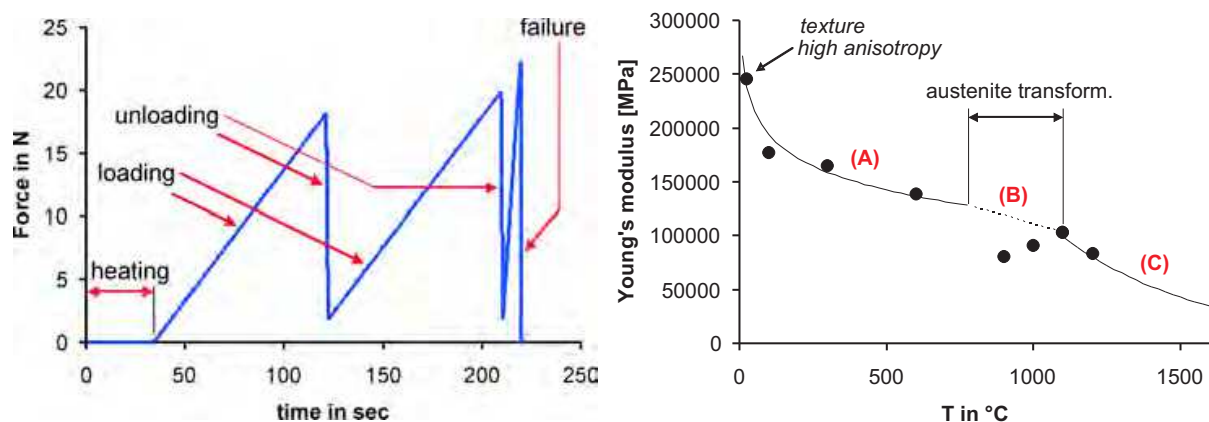


Fig. 15. *Left*: Illustration of (Un-)Loading by means of the force-time characteristics ($T = 100$ °C). *Right*: YOUNG's modulus vs. temperature with the following stepwise interpolations: (A) $E = -31938 \ln(T) + 340924$; (B) $E = 77.9\,T + 188811$; (C) $E = 10^7 \exp[-0.0021\,T]$.

the according values of $T = 20$ °C, i.e., $E = 246$ GPa, $R_{p02} = 760$ MPa, $R_m = 1102.4$ MPa und $A_g = 0.056$. The arbitrary parameter of Eq. (35) obtained by this method are $n = 0.1$ und $K = 1500$ MPa.

A visual comparison of the curves in Figure 13 (upper left) and 17 indicates the adequacy of both methods. The decision of which values will be experimentally determined depends on the experimental equipment and personal preferences.

## 4. Finite element simulations

### 4.1 Temperature distribution

The subsequent simulations exclusively refer to the caloric materials data of Section 3.1 as well as to geometry, discretization and side-/initial conditions of Section 2.5. In particular, the heat source macro LASIM provided by ANSYS® is applied, cf. Figure 6 (right), by using the following source geometry data:
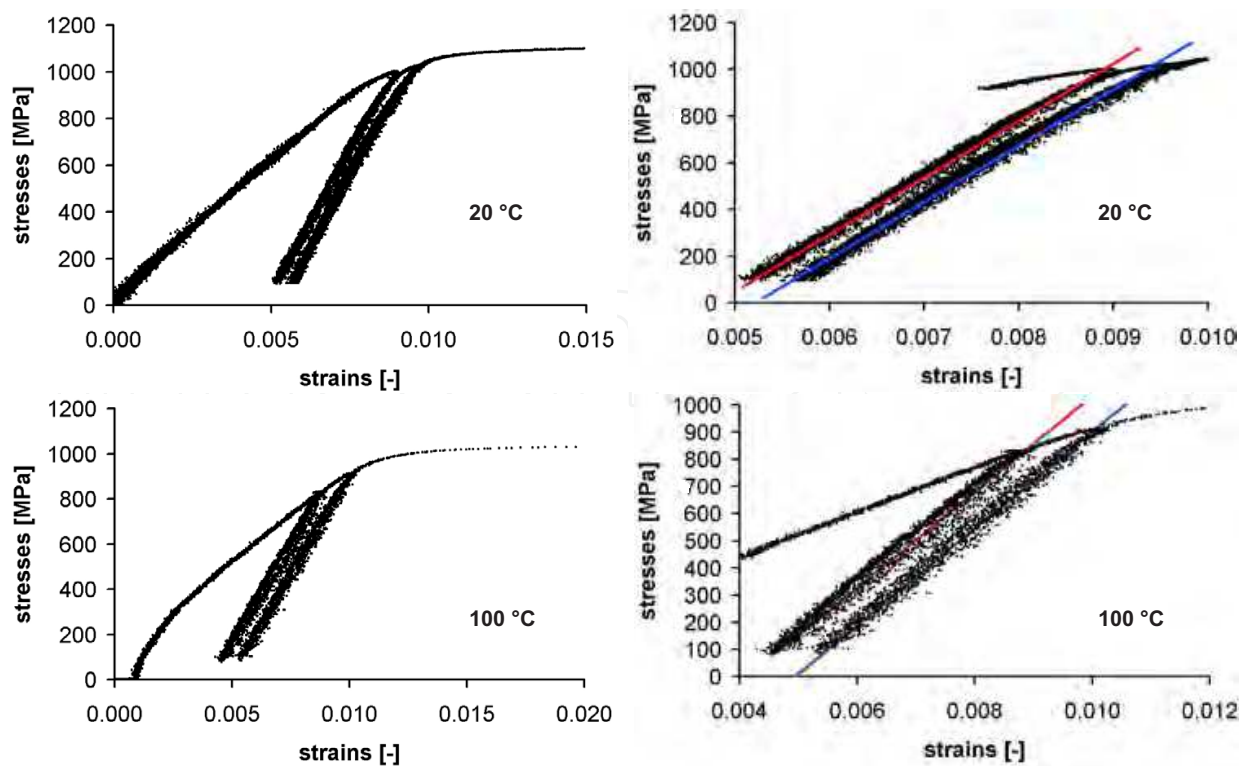
Fig. 16. Cyclic stress-strain history for $T = 20\,^\circ$C and $T = 100\,^\circ$C including a zoomed view on the unloading regime (right panel).
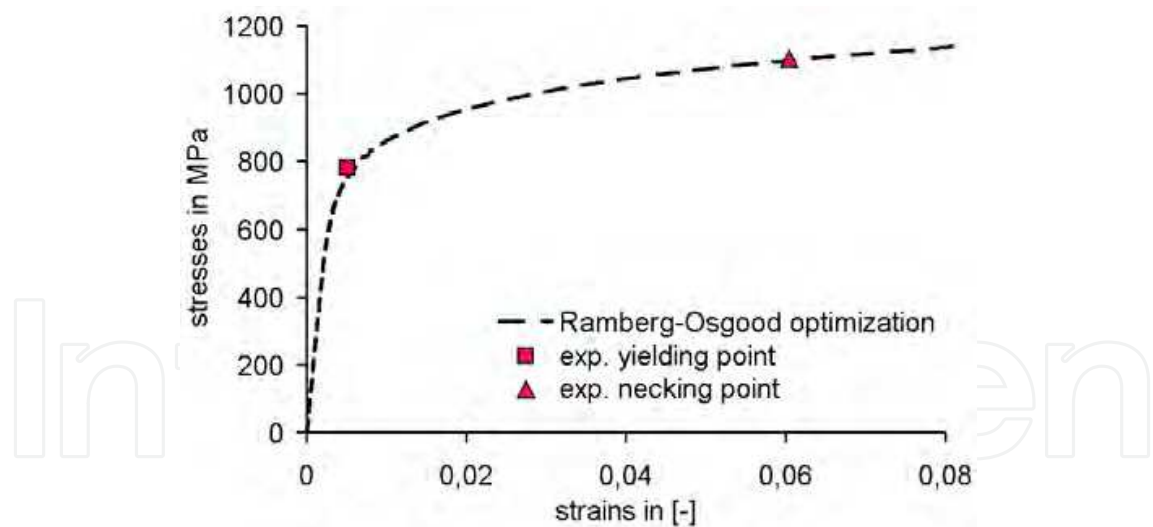


Fig. 17. Stress-strain curves for the as-rolled TRIP 700 steel at temperature $T = 25\,^\circ$C following from the optimization procedure and the RAMBERG-OSGOOD-ansatz.

With typical laser welding processes during steel manufacturing, such as continuous galvanizing, in mind, the welding parameters are used as follows:

$$v_s = 6\,\text{m/min} = 100\,\text{mm/s} \quad , \quad P_0 = 5\,\text{kW} . \tag{38}$$

Note, that Figure 10 partially contains data of different sources. In order to guarantee consistency with the phase transition temperatures of Figure 9 (and due to the 'moderate'

$$x_1^{\mathrm{f}} = 0.5 \text{ mm},\qquad x_2^{\mathrm{f}} = x_1^{\mathrm{f}},\qquad x_3^{\mathrm{f}} = x_1^{\mathrm{f}},$$
$$x_1^{\mathrm{r}} = 2.5 \times x_1^{\mathrm{f}},\qquad x_2^{\mathrm{r}} = 0.4 \times x_1^{\mathrm{r}},\qquad x_3^{\mathrm{r}} = x_2^{\mathrm{r}},$$
$$y_1 = 1.0 \text{ mm},\qquad y_2 = 0.8 \times y_1,\qquad y_3 = y_2,$$
$$z_2 = H/2,\qquad z_3 = H.$$

deviations) data exclusively calculated by JMATPRO are used. Thus the solid-liquid transformation temperatures are: $T_{\mathrm{solidus}} = 1457\ ^\circ\mathrm{C}$, $T_{\mathrm{liquidus}} = 1511\ ^\circ\mathrm{C}$. Figure 18 displays
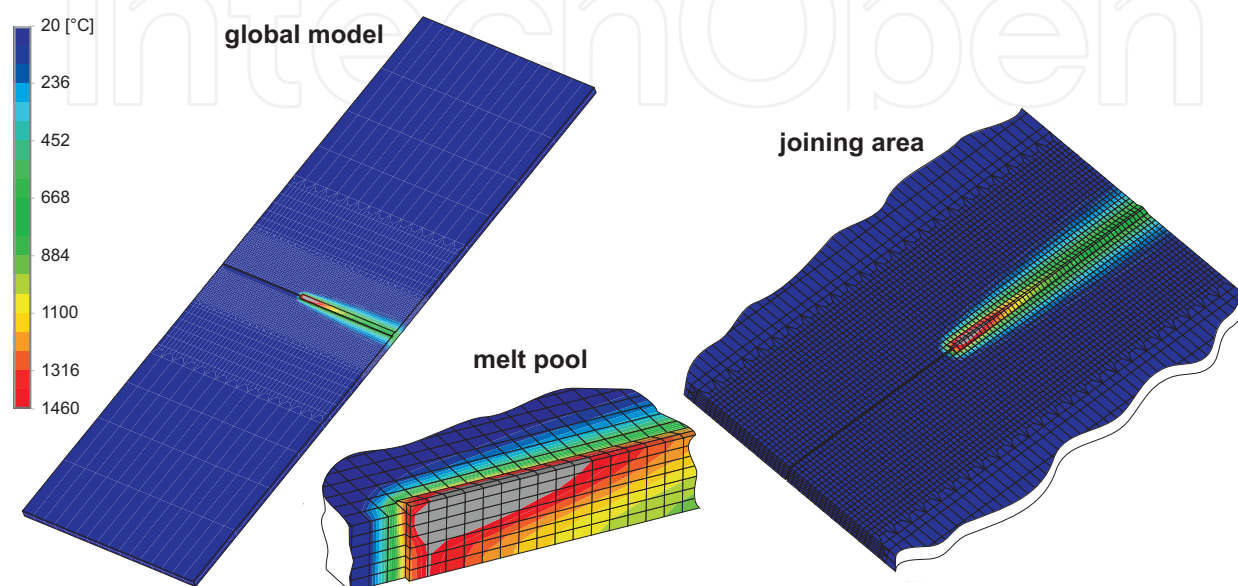


Fig. 18. Different contour plots of the thermal FE simulation including the cross-scetional view of the melt pool.

various contour plots of the thermal simulation after welding time of 0.26 s. As one can clearly see, gap elements will be activated, if one of its nodes achieves the melting temperature $T_{\mathrm{liquidus}}$. Figure 19 (left) compares the calculated melt pool geometry with the according, experimentally obtained, microphotograph. Obviously the a-priori assumed bulging behaviour is overestimated, whereas the calculated melt pool thickness is slightly thinner than the experimental one. However, in summary, there is an overall good agreement between the theoretical and realistic situation. Please note, such agreement is not self-evident, since no adjustments (e.g. of the heat input efficiency η) to experimental findings were used during simulation. Finally, Figure 19 (right) illustrates the calculated temperature vs. time curves of various, exemplary distances from the welding seam at the upper and lower side. The curves are similar to an asymmetric GAUSSian distribution, which is in agreement with purely mathematical formulations of the temperature distributions, (Elmer et al., 2001; Komanduri & Hou, 2000).

## 4.2 Distortion and residual stresses

The calculated temperature distribution is subsequently used to simulate the thermal deformation and, consequently, the resulting stresses and strains within the welded material. To this end the (thermo-) mechanical materials data, viz. $\alpha$ (cf. Figure 12, lower right), $E$ (cf. Figure 15, right), the stress-strain curves (cf. Figure 13), and POISSON's ratio $\nu = 0.3$ are applied. Furthermore (linear) 8-node hexahedral elements are chosen. Note, that during
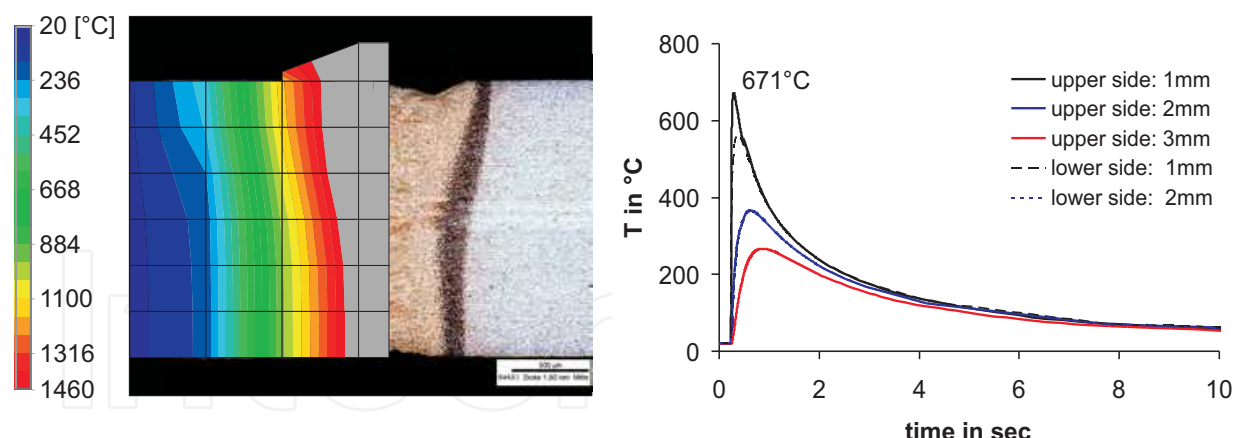
Fig. 19. *Left*: Comparison between calculated and experimentally observed weld pool geometry (sheet edge). *Right*: Calculated temperature vs. time dependence at different distances from the welding seam (upper and lower side, $x = L/2$).

the thermal simulation the initially deactivated gap- and bulging elements are activated as soon as **the melting temperature is reached** due to the heat conduction of the liquid matter. In contrast, the deactivated elements of the mechanical simulation are activated as soon as the reach the solidification temperature **after quenching**, since stresses exclusively develop within the solid state. Moreover, the thermal expansion of the activated elements must be calculated w. r. t. the reference temperature $T_{\text{solidus}}$, whereas the initially activated elements refer to the temperature before welding, i.e., $T_0$ (surrounding temperature). This fact can be realized by 'material changing' parallel to the element activation.

Furthermore it is worth mentioning, that the application of the `Ekill / Ealive` technique requires a sensible adjustment of the ANSYS® calculation option in order to guarantee convergence. In particular option for an adaptive time integration scheme, non-linear geometry, and the SPARSE solver is recommended.

In Figure 20 different contour plots of the VON MISES stress are presented to illustrate the developing stresses during joining as well as the remaining residual stresses after welding and cooling. Clearly to see is, first, the gap opening and, second, the considerable, tensile residual stresses within the welding seam after cooling. On the other hand the seam is nearly stress-free immediately after joining. The boundary regions at the beginning and the end of the welding area contain elevated residual stresses, in particular high compressive stresses in $y$-direction and tensile stresses in $z$-direction. This fact is indicated by the components of the stress vector at the material's surface illustrated in Figure 21. A comparison of the residual VON MISES stress with stress-strain curve in Figure 12 (at $T = 20$ °C) indicates a significant remaining stress level after welding, in particular at the middle of length ($x = L/2$). Here the illustrated stresses correspond to the qualitatively plotted distributions found in literature, e.g. (Voss, 2001).

The moving heat source leads to extremely short, positive or negative fluctuating strain amplitude, cf. Figure 22 (first and second row). Here the strain components at the upper side at distances $y = 1$ mm and 10 mm are displayed, which tend to stationary values for increasing time. The final strains resulting from the local thermal expansion are considerable smaller (and show partially opposite sign) at $y = 10$ mm than at 1 mm, which underscores the highly local impact of laser welding processes. This fact is also evident by considering
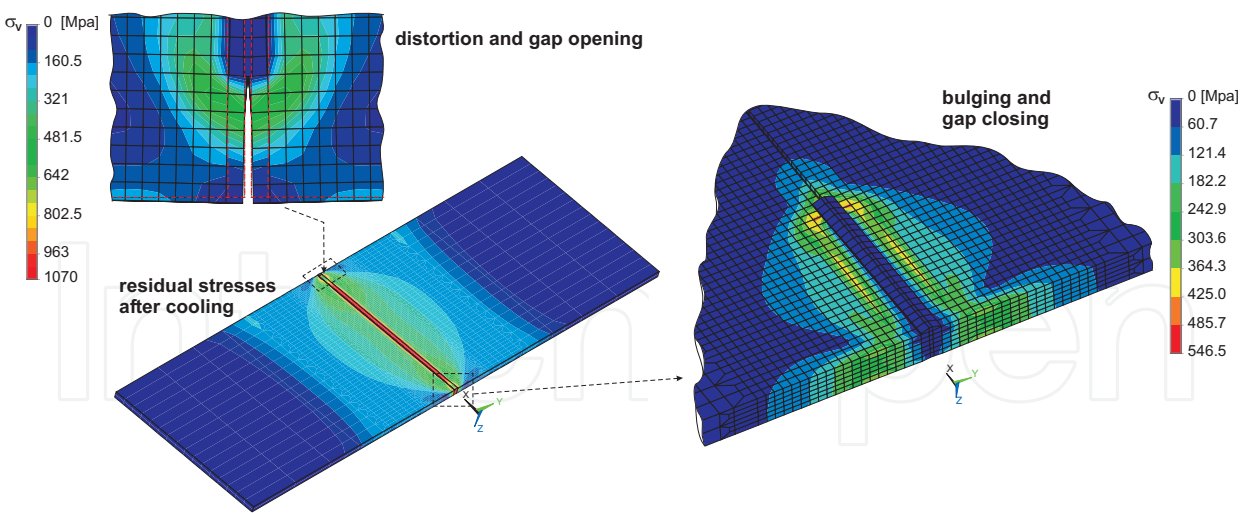
Fig. 20. Gap opening (scaling factor: 3) and VON MISES stress during and after welding of as-rolled TRIP 700.
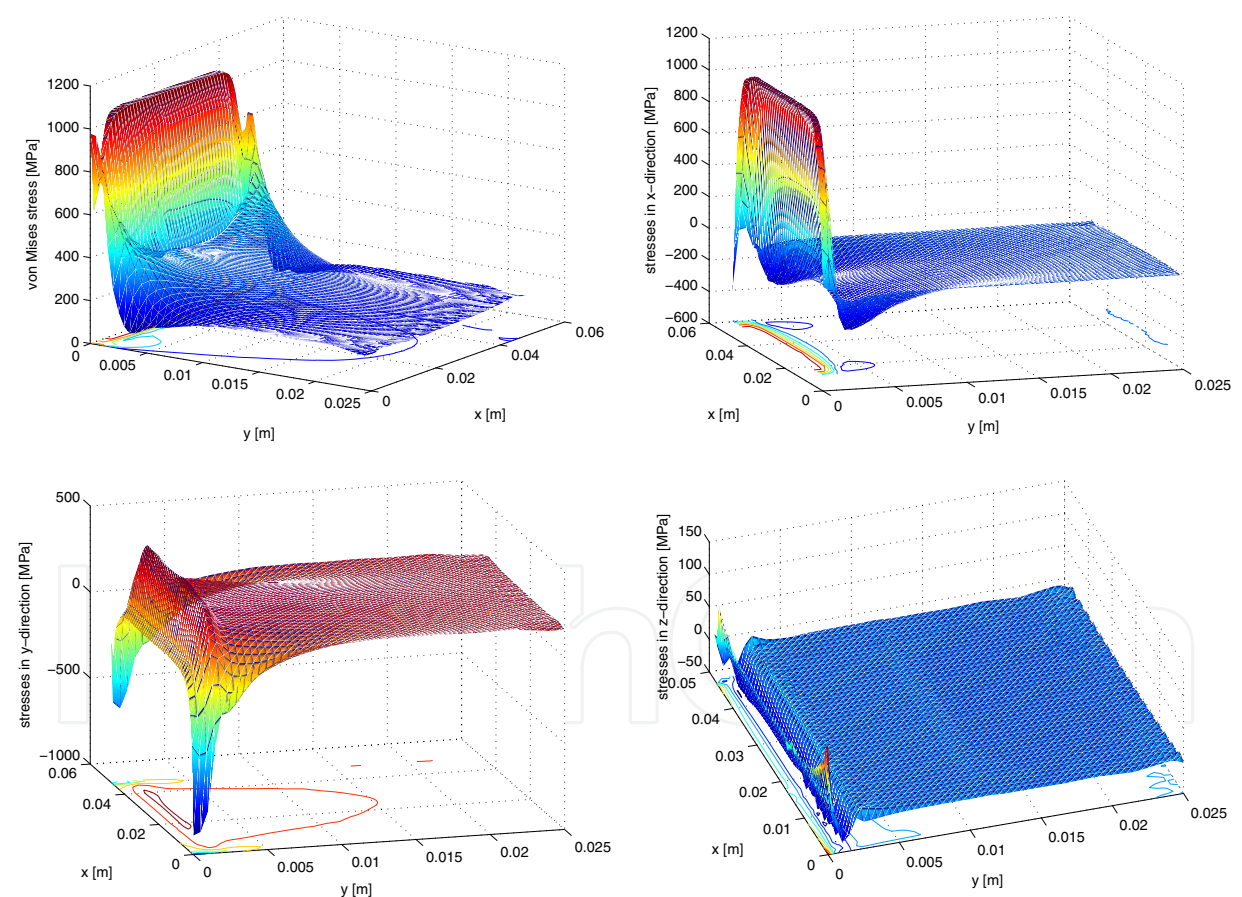


Fig. 21. 2D-distribution of the VON MISES stress and the stress-vector components at the surface after cooling.

Figure 22 (third row), in which most remarkable distortions are found within the first three millimetres beside the seam. Altogether one can say that the demonstrated FE-simulations represent a powerful tool to estimate the mechanical and thermal materials response. In detail
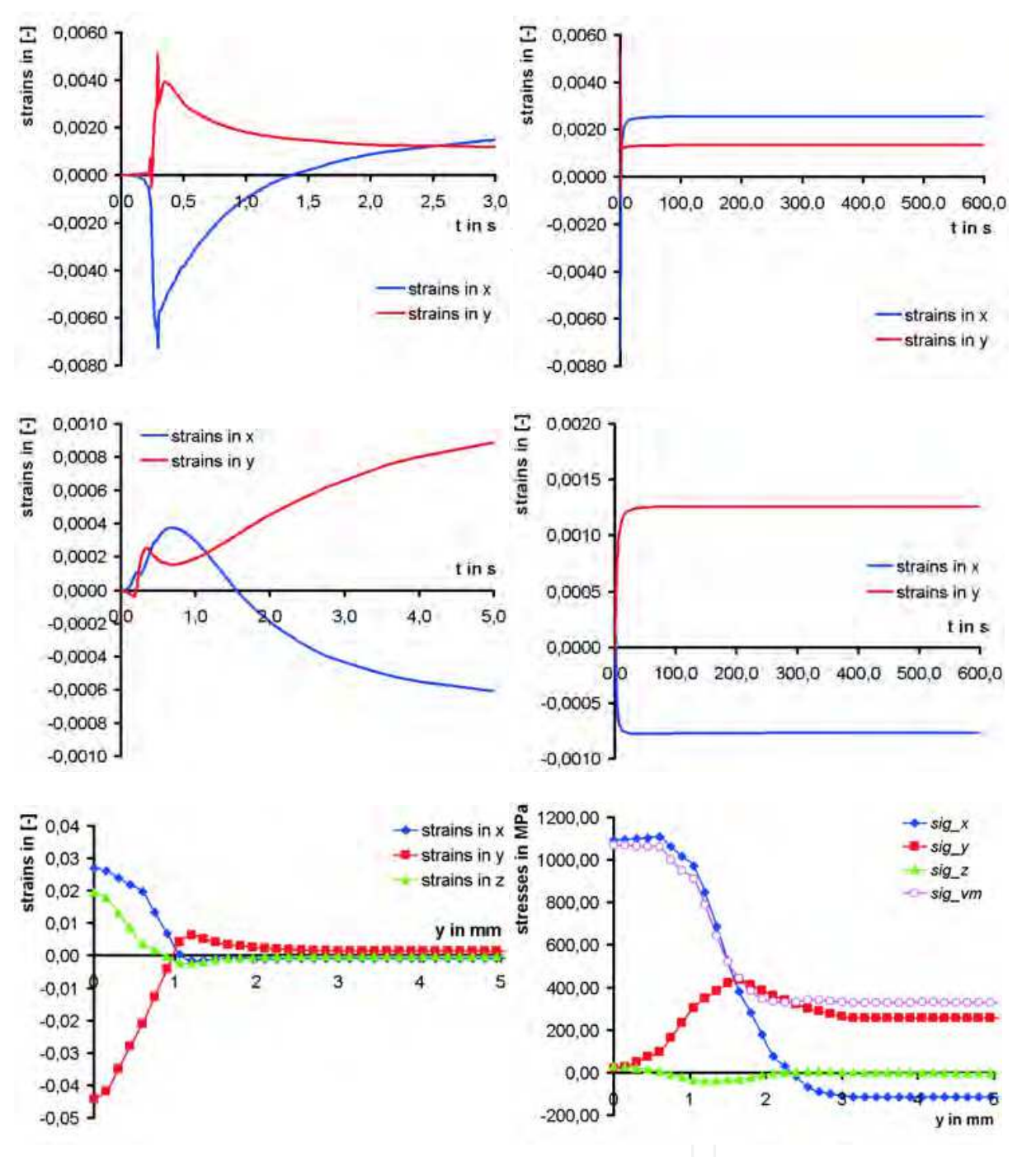
Fig. 22. *First and second row*: Temporal development of the components of the strain vector at the upper surface and at $(x, y) = (L/2, 1\,\text{mm})$ and $(x, y) = (L/2, 10\,\text{mm})$. *Third row*: cross-sectional distribution of the stress components at the upper surface and at $x = L/2$.

it is possible to calculate temperatures, strains, and stresses for arbitrary time and position. Critical regions and values can be identified, which may yield limitations for subsequent process parameters, such as strip tensions during continuous galvanizing, and materials combinations.

## 5. Experimental, comparative investigations

### 5.1 Welding experiments

Simultaneously to the numerical simulations experiments have been performed to measure temperatures and distortions at fixed, predefined positions. For this reason two similar sheet geometries[15] are used: $L \times W \times T = 100 \times 150 \times 1.8$ [mm] and $L \times W \times T = 50 \times 75 \times 1.8$ [mm] (geometry of the theoretical investigation). The corresponding specimens are assembled at the upper side (at $X = L/2$) with ThermoCouple Elements (TCE) at different distances to the welding seam as well as Strain Gauges (SGs), rotated by 90 ° to each other, to measure length- and transversal-displacements, cf. Figure 23 and 24. Thus the temperature over time is measured at $Y = 1$ mm, 2 mm, 3 mm and partially 6 mm (for $100 \times 150$ [mm] sheets). The displacements can only be integrally quantified along a finite length due to the dimension of the SG. Here changes of the length of a (rosette-type) fine wire, following from changes of the rosette's height, is exploited (in our case the height is $7 \ldots 11$ mm), cf. Figure 24. The
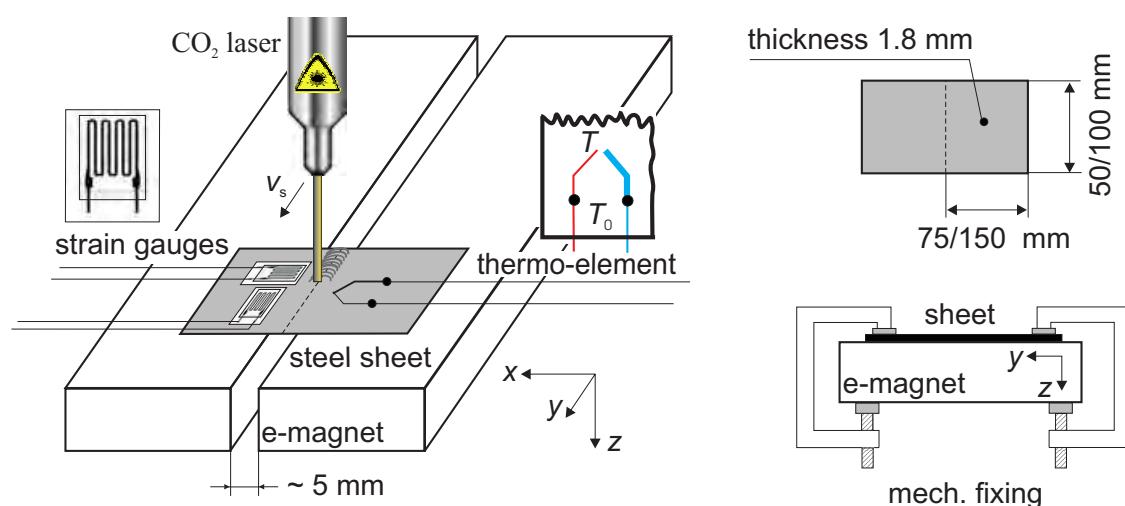


Fig. 23. Schematic view of the experimental setup for the determination of welding distortions and time-temperature curves at fixed distances from the welding seam.

measurement by TCE is based on the so-called SEEBECK effect, i.e. the development of voltage $U_m$ due to different temperatures at the two ends of an electrical conductor (e.g. wire). The TCE results by combining two conductors of different materials in series such, that the ends of both conductors are nearly situated at the position of same temperature. The following relation holds:

$$U_m = k_{AB}(T - T_0) \quad \text{with} \quad k_{AB} = k_A - k_B ,  \tag{39}$$

in which $T_0$ identifies the reference temperature, measured at the terminals of the voltmeter, and $k_{AB}$ quantifies the proportionality[16] between voltage and temperature difference of the two materials A / B. If $T_0$ and $k_{AB}$ are known and $U_m$ is measured at the ends of the metallic wires, the unknown temperature $T$ can directly be calculated via Eq. 39. In the present case CrNi-Ni wires of diameter $D = 0.3$ mm with $k_{CrNi} = 22$ V/K and $k_{Ni} = -19.4 \ldots -12$ V/K are used, (Feldmann, 2008). The underlying theory of SG-measurements follows from the

---

[15] The larger geometry is investigated to ensure the validity of the assumption of RSE, cf. Section 2.5.

[16] For considerable temperature differences the temperature dependence of $k_{AB}$ is not negligible. Then a polynomial ansatz of the form $k_{AB}(T) = a + bT + cT^2 + \ldots$ can be used, which yields a nonlinear relation for $T$ in Eq. (39).
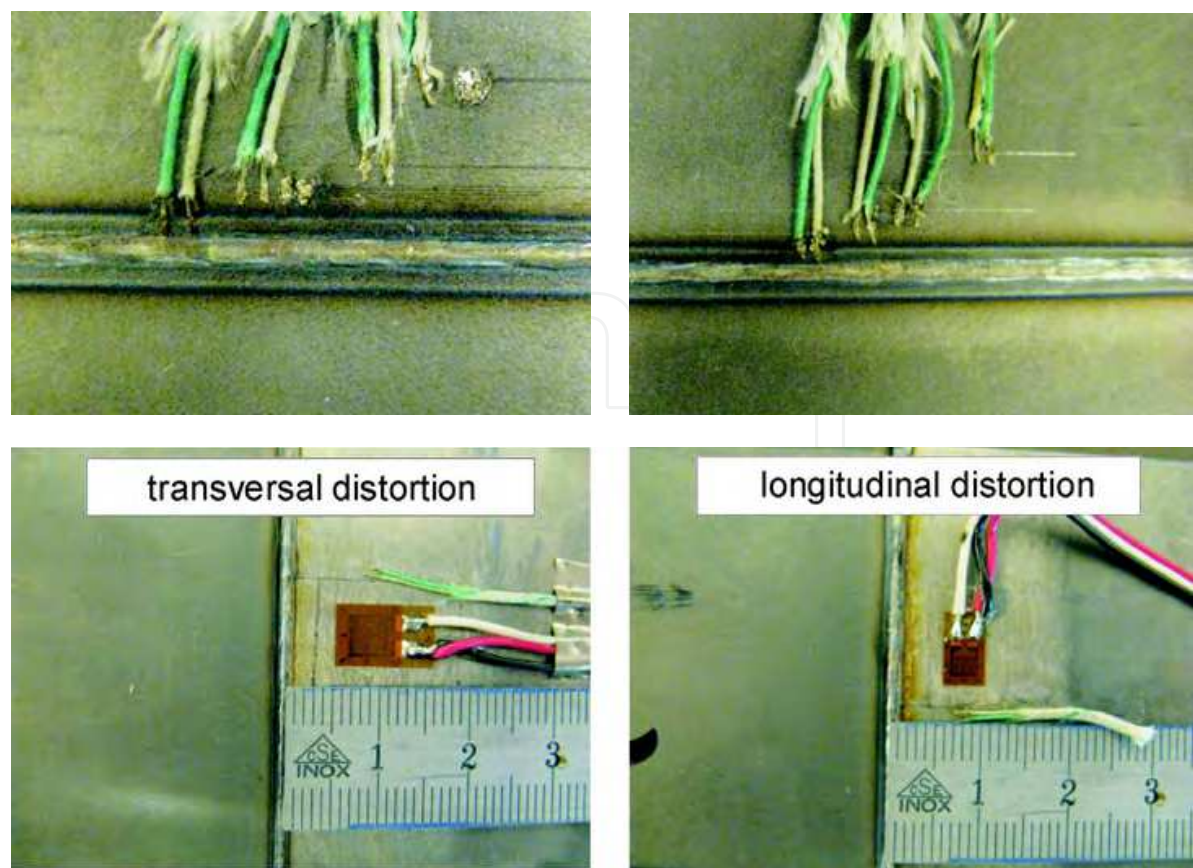
Modeling, Simulation and Experimental Studies of Distortions,
Residual Stresses and Hydrogen Diffusion During Laser Welding of As-Rolled Steels

101

Fig. 24. *First row*: position of the TCEs at the upper side: 1 mm, 2 mm, 3 mm, and 6 mm (for the $150 \times 100$ [mm] specimen) beside the seam. *Second row*: position of SGs: $7 \ldots 11$ mm (transversal) or $7 \ldots 10$ mm (longitudinal) beside the seam.

observation that changes of the length $\Delta l$ of a cylindrical wire lead to the reduction of its electrical resistance $R$:

$$\frac{\Delta R}{R} = \hat{k} \frac{\Delta l}{l} \quad \text{with} \quad R = \frac{4 l \rho}{\pi D^2} \; . \tag{40}$$

By means of the relation $\Delta R = (\partial R / \partial l) \Delta l + (\partial R / \partial \rho) \Delta \rho + (\partial R / \partial D) \Delta D$ one finds:

$$\frac{\Delta R}{R} = \frac{\Delta l}{l} + \frac{\Delta \rho}{\rho} - 2 \frac{\Delta D}{D} \; . \tag{41}$$

By comparing Eq. $(40)_1$ and (41) and by assuming the metal-specific approximation $\Delta \rho = \Delta V = 0$ a value of $\hat{k} = 2$ is derived, which represents 'a standard value' due to the introduced assumptions. Usually $\hat{k}$ values are reported by the provider and manufacturer of the SGs, for e.g. wires made of constantan holds $\hat{k} = 2.05$.

Finally it is worth mentioning, that SGs typically fixed at the (metallic) surface by polymer adhesives, which guarantee the reliable joining up to the critical temperature of 200 °C in the present case. Consequently the SGs must be positioned beyond a critical distance from the welding seam, which is found by the preliminary TCE measurements.

In Table 3 the performed eight experiments are summarized. The joining process is realized by the parameters, listed in Eq. (38). Furthermore a Helium shielding gas is used, and the sheets

| no. | quantity of interest | no. of tests | geometry [L $\times$ W] |
|---|---|---|---|
| 1 | temperature | 2 | $50 \times 75$ mm |
| 2 | distortion (transversal) | 1 | $50 \times 75$ mm |
| 3 | distortion (longitudinal) | 1 | $50 \times 75$ mm |
| 4 | temperature | 2 | $100 \times 150$ mm |
| 5 | distortion (transversal) | 1 | $100 \times 150$ mm |
| 6 | distortion (longitudinal) | 1 | $100 \times 150$ mm |

Table 3. List of performed welding experiments.

are magnetically and mechanically fixed as indicated in Figure 23 and 25. The measured time-temperature curves at the TCEs of the test series 1 and 4 are displayed in Figure 26 (first row). Here two measurements are exploited for each series in order to find the mean square deviation $\Delta$ via the relation $\Delta = [T_1(t_i) - T_2(t_i)]^2$, cf. Figure 26 (second row). By means of the quantity $\sqrt{\Delta}/2$ the error bars, illustrated in Figure 26 (last row), can be derived. The experimentally obtained welding strains at the upper side and $X = L/2$ are displayed in
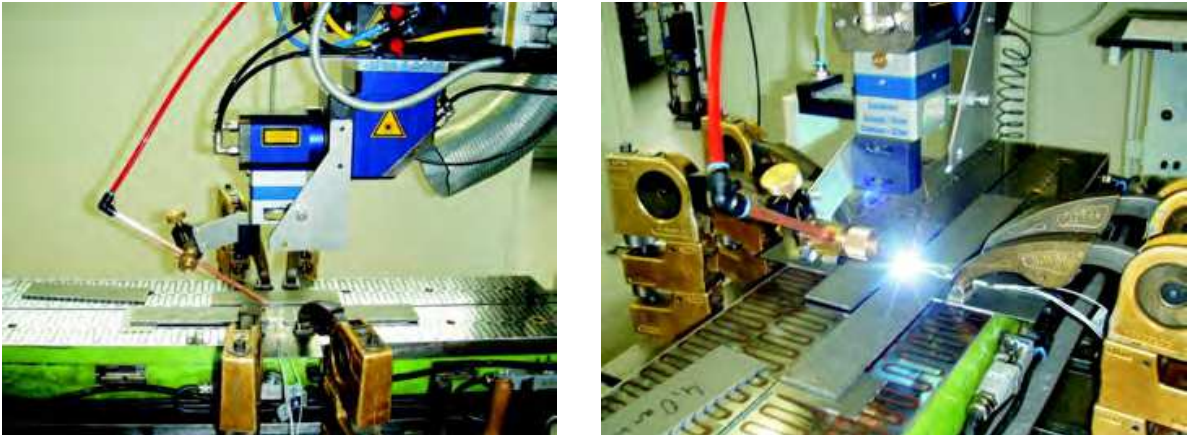


Fig. 25. Illustration of the laser welding equipment (CO2) and the mechanical fixation.

Figure 27. Here the first row shows the longitudinal strains and the second row the transversal strains, $7 \ldots 10$ or $7 \ldots 11$ mm beside the seam, respectively. The geometry of the used strain gauges is $L \times W = 1.6 \times 3.1$ mm (series 2-3) and $3.2 \times 4.6$ mm (series 5-6). Obviously, the final residual strains, characterized by the stationary values, are obtained after 40 s. Furthermore the starting point of the measurements slightly varies. Consequently there is a time shift between the different experimental curves. However, this 'shift' has no physical meaning and is cancelled for a better comparison.

As one can easily see, there is a qualitatively and (mainly) quantitatively excellent agreement between the distortion curves of different geometry. This fact is not self-evident but underscores the validity of the RSE assumption. The deviation in the upper left figure results from the preterm release of the mechanical fixation (blue curve). Finally, we did not perform a second comparative measurement to save time and materials.

### 5.2 Theory vs. experiment

First of all, we compare the temporal temperature evolution following from the numerical simulation and the TCE measurement, cf. Figure 28. In fact, there are slight deviations between the theoretical and experimental peak temperature, however, the overall agreement,
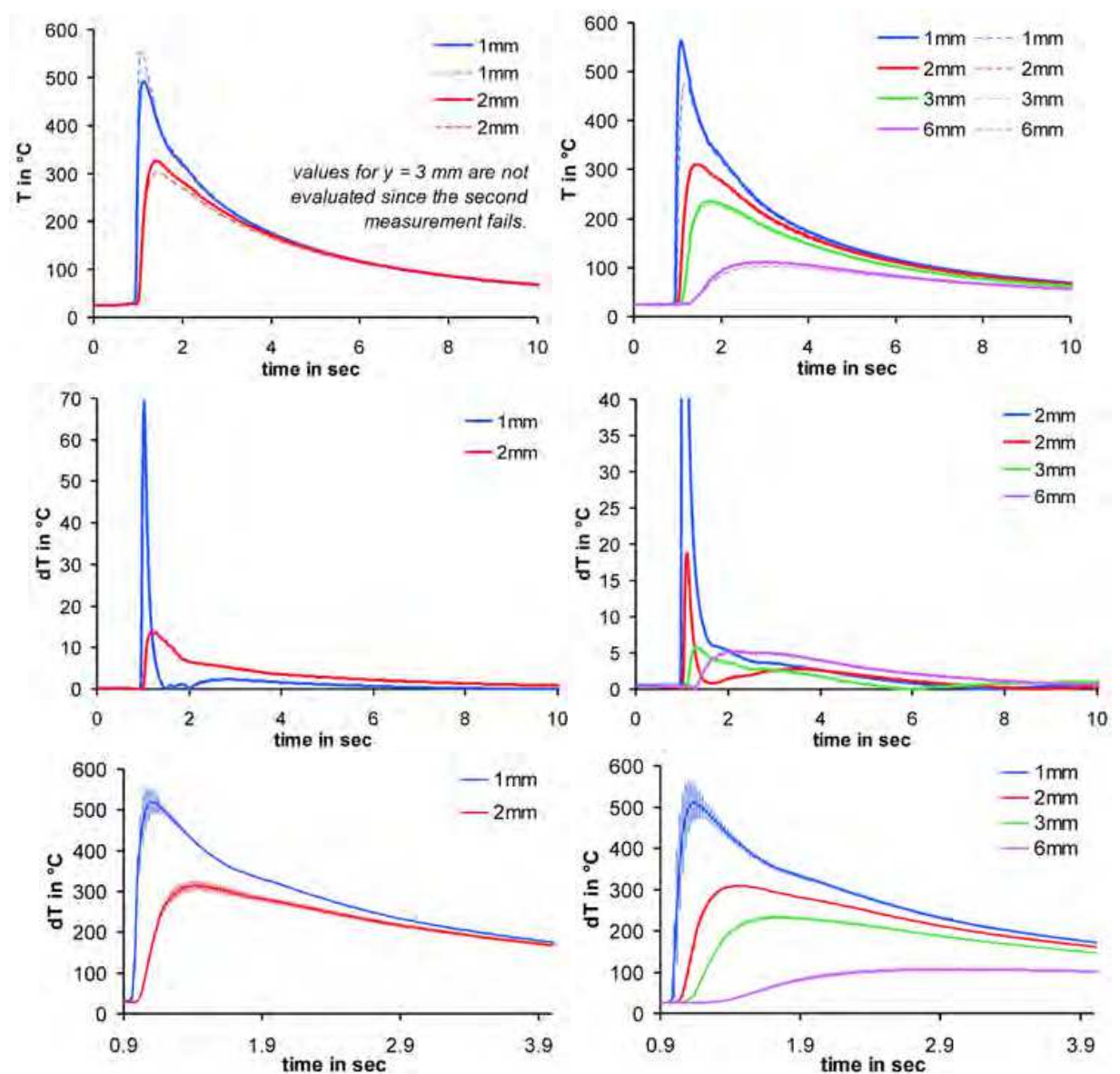
Fig. 26. Temporal temperature evolution at the TCEs for series 1 (left) and 4 (right). *Upper row*: origin data; *Middle row*: mean square deviation ; *Last row*: time-temperature dependence with error bars.

in particular during cooling, is excellent. Two main reasons can be found for the discrepancy of the maximal temperatures (plain vs. dashed lines):

**(a)** The TCE shows certain initia behaviour, due to the used sample rate of 50 Hz. Thus, values are 'only' registered within the time increment of 0.02 s, whereas the used spatial discretization of the simulation yields a time step of 0.005 s (required time to move the centre of heat source in $x$-direction one node forward).

**(b)** Measurements by TCE require additional metallic material, i.e. the TCE wires, at the surface of the specimen, which causes additional cooling and heat transfers. Therefore reduced temperatures are measured at the TCE.
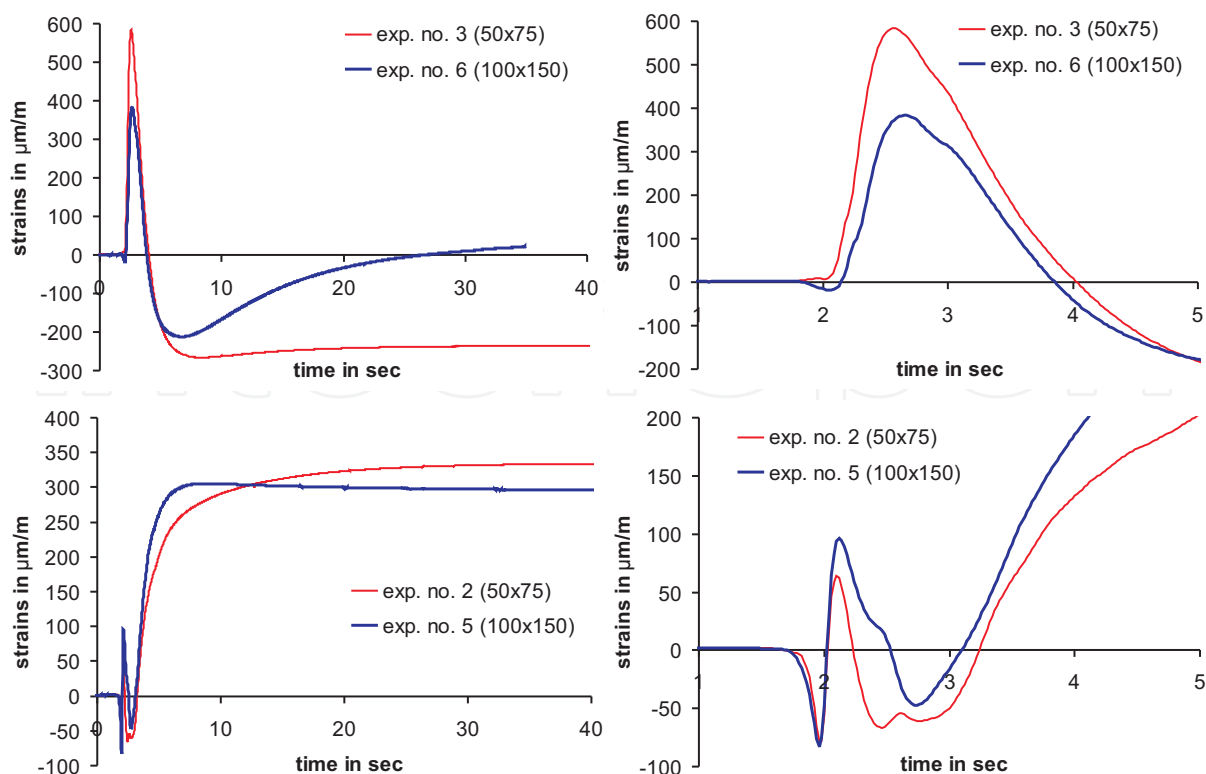
Fig. 27. Experimental results of the SG measurements. *Left*: Time-strain curves up to the stationary state. *Right*: Zoomed view onto the initial process.

Figure 29 compares the experimental and calculated time-strain relations, analogously to the illustration in Figure 22 and 27, at the lateral welding seam distance of 11 mm (sheet geometry $L \times W = 50 \times 75$ [mm], upper side, $X = L/2$). It is easily to see, that the theoretically predicted curves qualitatively follow the experimental ones. Moreover, the calculated stationary strains of the $x$-direction also render the reality in a quantitative manner. Deviations mainly occur for the stationary values of lateral strains (by factor 3.5 - 4) and for the strains during joining (i.e. the initial fluctuations). In particular, one finds an underestimation for the initial, fluctuating strains in $x$-direction and an overestimation in $y$-direction w.r.t. the experiments. To identify the reason of these deviations, one firstly tends to identify the mechanical boundary conditions to be not sufficiently realistic, cf. Figure 8. Especially the upper-side fixation of the sheet is wider and shows an opening for the SG and required cable routings, see Figure 25.

However, this interpretation is in contradiction with the good agreement of the theoretical and experimental values in $x$-direction. Consequently, unrealistic boundary conditions cannot be the sole origin of the above discrepancy. A second reason - and eventually the main reason - is given by the used, isotropic mechanical materials data. As-rolled steel contains a strong rolling texture and, therefore, a high anisotropy follows. Orientation-depending materials data, e.g. for YOUNG's modulus or expansion coefficient, are required, which require extensive mechanical testing, especially of specimen with different rolling directions. Additionally, one may take an anisotropic yield criterion, such as HILL's yield surface, into account, (Ansys theory ref., 2007).

Finally it should be mentioned, that SG measurements allow for documentation of the temporal strain evolution with certain locality (dimension of the SGs). In contrast, distortion
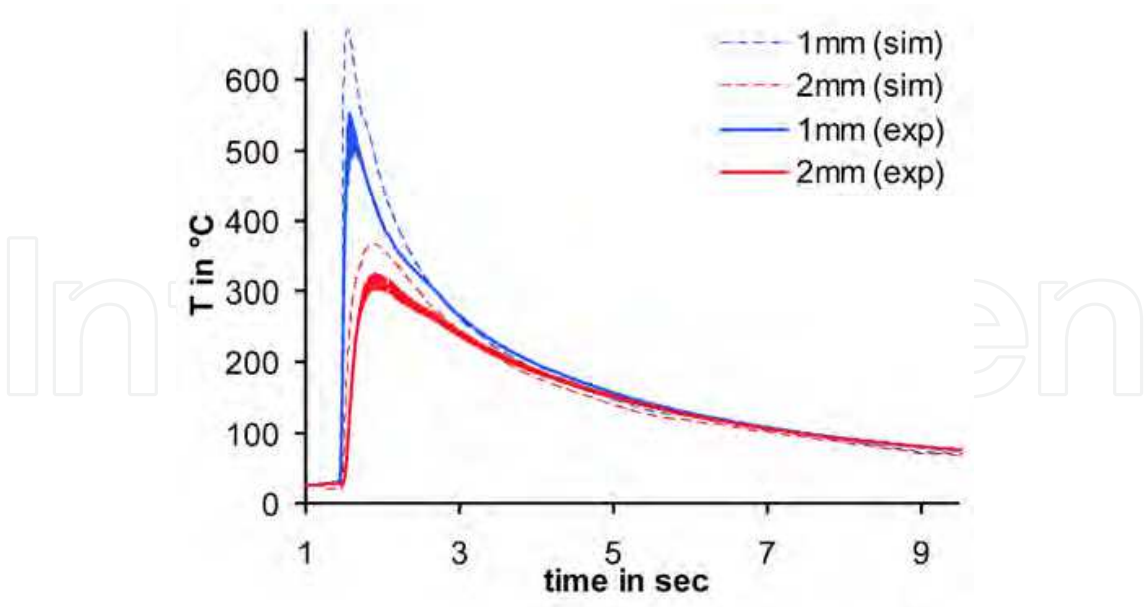
Fig. 28. Experimental vs. theoretical time-temperature curve, distance from the welding seam: 1 mm and 2 mm (upper side).
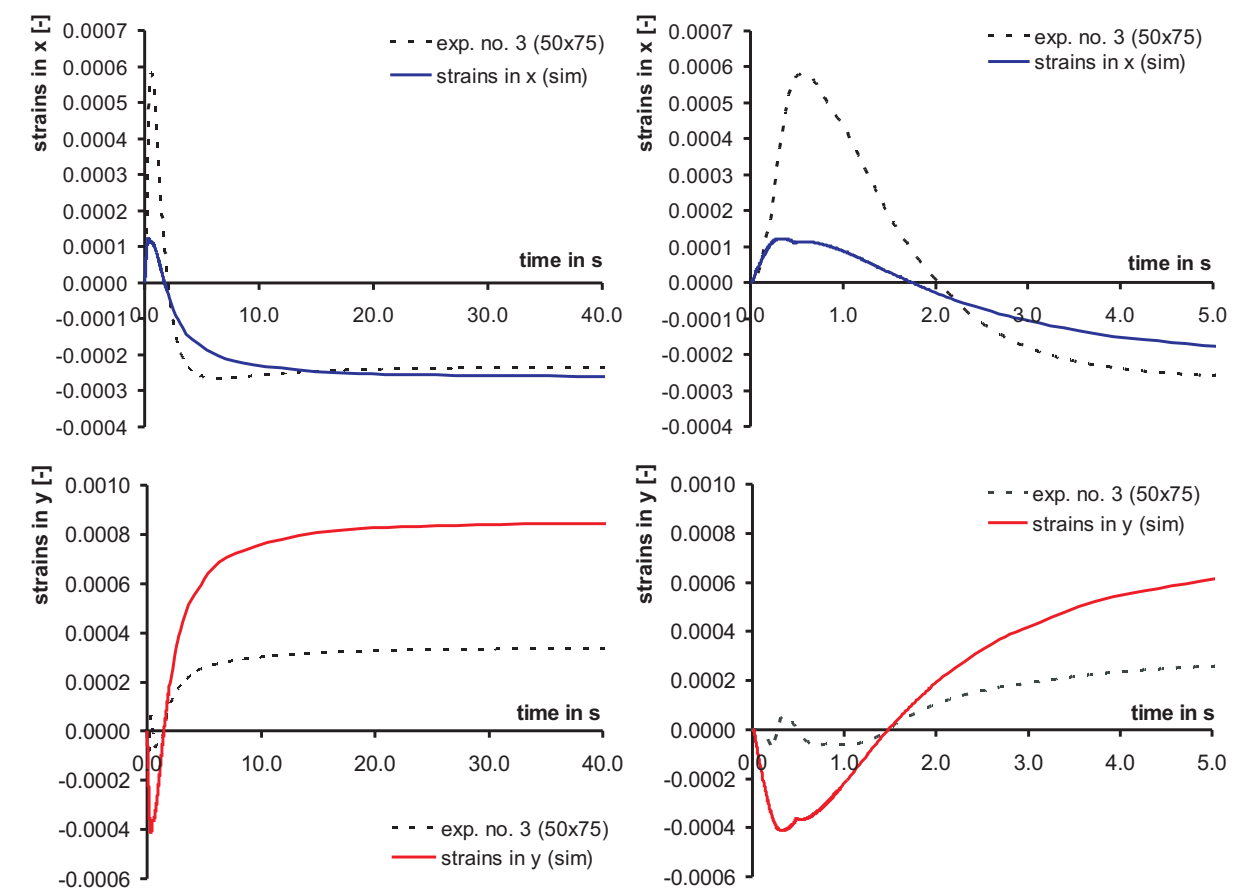


Fig. 29. Comparison between calculated ($y = 10$ mm) and measured ($y = 8 \ldots 12$ mm) mechanical response. *Right*: Zoomed view onto the initial process.

measurements via displacement transducers at the boundaries of the sheet, such as in (Voss, 2001), 'only' yields integral values.

## 6. Discussion: possibilities and limitations

### 6.1 Phase transformations

Heat input and welding-induced stress fields yield to changes of the microstructure, cf. Figure 30. This complex phenomenon is mainly triggered by four factors, viz.:

**a.** initial microstructure (e.g. ratio of retained austenite),

**b.** heating and cooling rates,

**c.** peak and final temperature (the latter one is usually the room temperature),

**d.** distortions and stresses (resulting, e.g. from TRIP effects).

For instance, variations of the content of retained Austenite (A) within the origin microstructure before welding yield different amounts of A within regions of partial austenitization (within the $Ac1$ - $Ac3$ temperature regime). On the other hand different, final Ferrite (F) or Bainit (B) contents result for varying quenching rates, cf. Figure 31[17]: $t_{8/5} = 4$ s vs. $t_{8/5} = 40$ s or B-M vs. F-B-M composition, respectively. Two kinds of microstructure changes can be identified:

**1.** variations of composition, i.e. of A-, F-, B-, and Martensite (M) contents,

**2.** changes of the micro-morphology, namely of grain size or phase shape/size.

Changing microstructures influent the thermodynamic and mechanical properties of the material, and may considerably determine resulting welding distortions and residual stresses. Martensite formation in the vicinity of the welding seam due to high cooling rates, for example, lead to increasing volume and to additional, positive strains, (Dean & Hidekazu, 2008). A second example is grain growth within the Heat Affected Zone (HAZ), which reduces the strength of the origin fine-grained material, cf. Figure 30 (region B). From the point-of-view of modelling and simulation physical models and mathematical methods are required, which allow to quantify the changes of item **1.** and **2.** depending on the factors denoted under **a.** - **d.**. However, due to the high complexity of matter, only theoretical investigations of single aspects are found in literature. One of the most established[18] models for estimating phase changes during welding are the so-called JOHNSON-MEHL-AVRAMI-KOLMOGOROV (JMAK) ansatz, (Avrami, 1939; 1940), for diffusion-induced transformations (Bainit ↔ Ferrite ↔ Austenite) and the KOISTINEN-MARBURGER[19] (KM) model, (Koistinen & Marburger, 1959), for diffusion-less phase formations. Beyond these the following models are worth-mentioning:

**Leblond**:
*Here a differential equation for the description of nonisothermal, diffusioninduced and -less transformations is derived. Furthermore the model allows for the prediction of the temporal grain size evolution, (Leblond & Devaux, 1984).*

---

[17] The graph exclusively holds for the present material and indicated experimental conditions.

[18] One of the reasons is the simple mathematical formulae, resulting in manageable computational efforts.

[19] Surprisingly, this highly cited work is a short comment, in which experimental results are presented and fitted by an obviously universal, linear function.
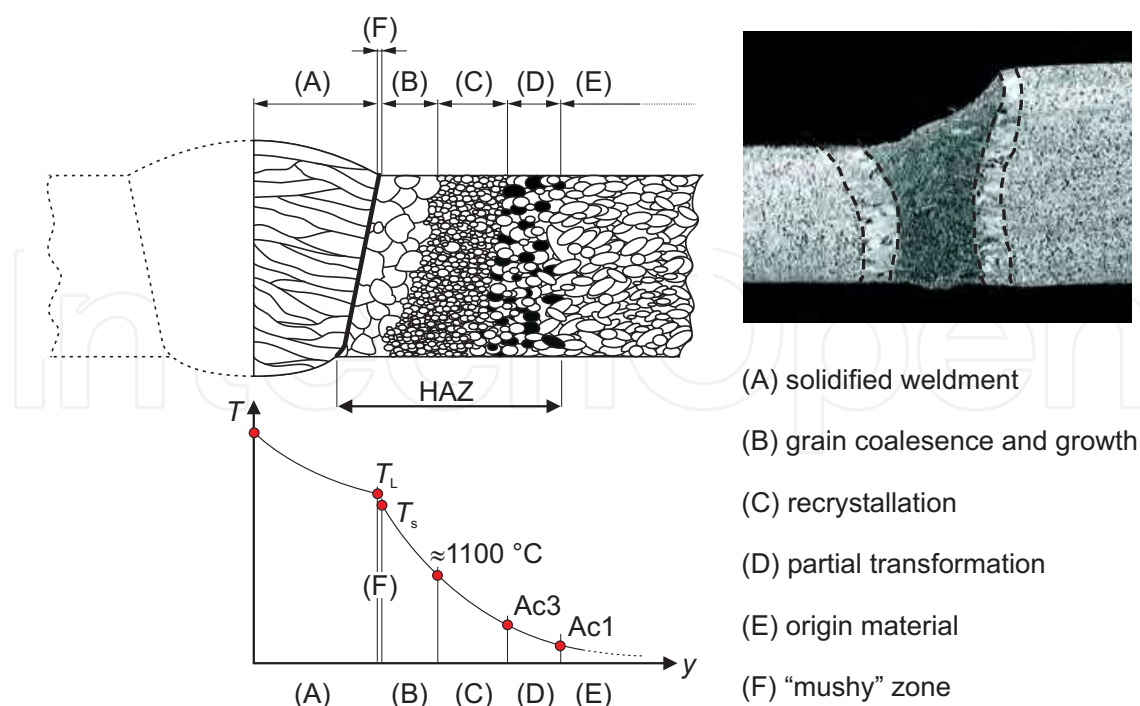
Fig. 30. Schematic illustration of different microstructures within the lateral joining region, following from (Francis et al., 2007); photo by courtesy of O. Voss (TK Tailored Blanks S.A. de S.V., Puebla, Mexico).

**Cahn-Hilliard:**
*So-called phase field models can be used to describe the local evolution of micro-morphologies. This approach is the most general one; but considerable computational efforts are required and materials data as well as initial/boundary conditions are often unknown, (Cahn & Hilliard, 1958; Cahn, 1961; Thiessen et al., 2007).*

**Zener:**
*This historical work provides a model to describe the evolution of the so-called growth coordinate (e.g. the phase radius in 3D) for isothermal, diffusion-induced transformations; ratios of different coexisting phases and morphologies are not considered, (Zener, 1949).*

**STAAZ:**[20]
*Here the different phases are experimentally determined and the resulting phase regions are plotted within a peak-temperature (y-axis) / cooling time (x-axis) diagram. Thus, correspondingly to the point-wise different heat treatment during welding, the various, calculated temperature histories can be used to identify points, and consequently phases, within the diagram, (Ossenbrink & Michailov, 2007; Ossenbrink, 2008; Voss, 2001).*

In what follows we briefly explain the strategy for calculation of welding induced phase transformations by using the JMAK and KM formalism. By assuming spherical (phase-)shapes and the so-called 'isokinetic regime' (isothermal boundary conditions) the model of JMAK applies methods of statistical physics to derive the following relations for

---

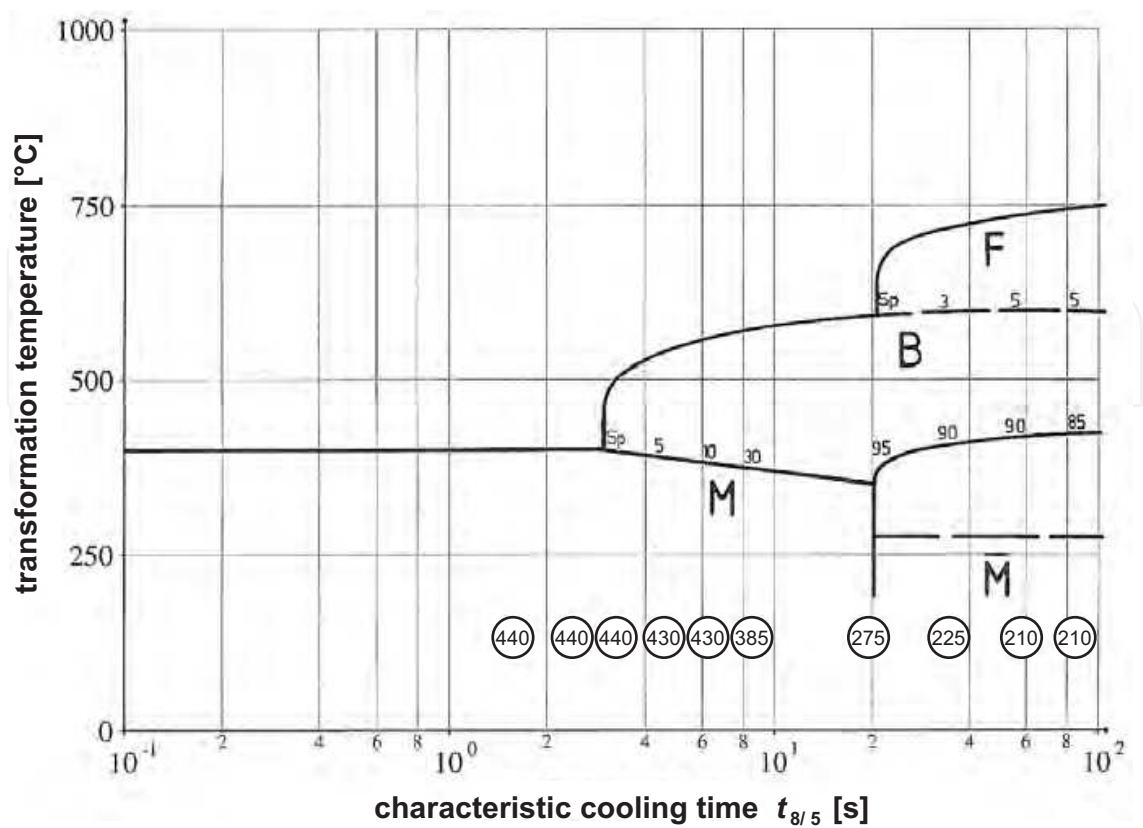[20] german abbreviation for: Spitzentemperatur-Austenitisierung-Abkühlzeit.

Fig. 31. Continuous-Cooling-Transformation (CCT) diagram for TRIP 700 (measured at Gleeble3500®). The following experimental procedure/material is used: heating (austenitization) up to 1350 °C, holding time: 1 s, $dT/dt = 337.5$ °C/s, austenite grain size: 3.0 (ASTM E112), material: cold rolled strip, thickness: 1.8 mm, $Ms = 400$ °C, $Ac1 = 735$ °C, $Ac3 = 1000$ °C.

the volume fractions of the different phases, (Avrami, 1940):

$$\xi^\gamma(t_i) = 1 - \exp\left[-a\, t_i^b\right] \quad \text{with} \quad \gamma = \{A, B, C\}. \tag{42}$$

Here $t_i$ represents the $i$-th time step of the FE calculation and $\gamma$ stands for the different, developing phases. The material-specific parameters $a$ and $b$ must be fitted to Time-Temperature-Transformation (TTT) diagrams[21], (Kang & Im, 2007). Furthermore the non-isothermal conditions during welding must be taken into account. For this reason, the continuous cooling process is divided into a monotone decreasing step function, and isothermal conditions are assumed for each single plateau. Note that Eq. 42 allows for a separate calculation of the different phases; but, realistically, they coexist and interact each other. In order to correctly combine the calculated volume fractions the so-called additivity rule, (Umemoto et al., 1982; 1983) must be used (detailed explanations can be found e.g. in (Dean et al., 2008; Dean & Hidekazu, 2008; Kang & Im, 2007)). This framework allows to calculate the volume fractions, $\xi^{A/F/B}$, of each element or node; but the micro-morphology remains undetermined.

---

[21] To prepare such diagrams the specimen is totally austenitized and subsequently quenched to the target temperature. Then the phase transformation is measured at constant temperature conditions. In contrast CCT-diagrams characterize the phase transformations for constant, predefined cooling rates.

The model of KM, especially in case of M-formation, states, that the volume fraction of the forming phase exclusively depends on degree of undercooling, namely:

$$\xi^{\mathrm{M}}(t_i) = 1 - \sum_{\gamma=\{\mathrm{B,F}\}} \xi^{\gamma}(t_i) - \underbrace{\left\{1 - \exp\left[-c(M_s - T_i)\right]\right\}}_{=\xi^{\mathrm{A}}}, \tag{43}$$

in which $M_s$ indicates the starting temperature of Martensite formation, $c =$ konst. $= 0.011$, $T_i$ stands for the present temperature at time $t_i$, and $\xi^{\gamma}$ denotes the volume fraction of the $\gamma$-th (non-martensitic) phase accordingly to Eq. (42)$_2$. Thus it is possible - starting from the (known) local fractions of A, F, B - to determine the fraction of M formed during the cooling period of the FE-analysis. However, information about the micro-morphology is not derived.

During laser-beam welding extremely high heating and cooling rates occur. Therefore partial austenitization and $t_{8/5}$-times between $0.8 \ldots 1.5$ s result, cf. Figure 28. Consequently the F- and B-areas of Figure 31 are not passed. For this reason it is sufficient to exclusively investigate the M-formation as a first step. Note that the phase evolution takes place on the micro-scale, whereas the used FE-mesh is suitable to simulate the macroscopic welding process. A finer discretization is required, which lead to unmanageable computational times in case of the present full 3D-geometry: A compromise could be the strategy summarized in Table 4:

The final phase composition can be used, for instances, to determine the lateral distribution of hardness (e.g. VICKERS). For this reason the following empirical equations hold, (Voss, 2001):

$$HV_{\mathrm{M}} = 127 + 949\,\mathrm{C} + 27\,\mathrm{Si} + 11\,\mathrm{Mn} + 8\,\mathrm{Ni} + 16\,\mathrm{Cr} + 21\,\mathrm{Log}(\dot{T})\,,$$

$$HV_{\mathrm{B}} = 323 + 185\,\mathrm{C} + 330\,\mathrm{Si} + 153\,\mathrm{Mn} + 65\,\mathrm{Ni} + 144\,\mathrm{Cr} + 192\,\mathrm{Mo} +$$
$$+ (89 + 53\,\mathrm{C} - 55\,\mathrm{Si} - 22\,\mathrm{Mn} - 10\,\mathrm{Ni} - 20\,\mathrm{Cr} - 33\,\mathrm{Mo})\mathrm{Log}(\dot{T})\,,$$

$$HV_{\mathrm{F/P}} = 42 + 223\,\mathrm{C} + 53\,\mathrm{Si} + 30\,\mathrm{Mn} + 13\,\mathrm{Ni} + 7\,\mathrm{Cr} + 19\,\mathrm{Mo} +$$
$$+ (10 - 19\,\mathrm{Si} + 4\,\mathrm{Ni} + 8\,\mathrm{Cr} + 130\,\mathrm{V})\mathrm{Log}(\dot{T})\,,$$

$$HV_{\mathrm{tot}} = HV_{\mathrm{F/P}}\,(\xi^{\mathrm{F}} + \xi^{\mathrm{P}}) + HV_{\mathrm{B}}\,\xi^{\mathrm{B}} + HV_{\mathrm{M}}\,\xi^{\mathrm{M}}\,. \tag{44}$$

Here $\dot{T}$ must be calculated at temperature of minimal stability for austenite, viz. $T \approx 500$ °C. To investigate the mechanical response of the material following from welding and the induced phase transformations, mechanical materials models are required, in fact before the mechanical FE analysis. Such models allow for the decomposition of the strains by incorporating the phase evolution, $\underline{\underline{\varepsilon}} = \underline{\underline{\varepsilon}}^{\mathrm{el}} + \underline{\underline{\varepsilon}}^{\mathrm{pl}} + \underline{\underline{\varepsilon}}^{\mathrm{th}} + \underline{\underline{\varepsilon}}^{\mathrm{A}\to\mathrm{M}}$. Here $\underline{\underline{\varepsilon}}^{\mathrm{A}\to\mathrm{M}}$ identifies the strain tensor due to the A-M transformation[22], (Dean et al., 2008; Dean & Hidekazu, 2008). It can be quantified by means of crystallographic arguments and the obtained, above volume fractions $\xi^{\mathrm{M/F/B/A}}$. In case of the commercial FE- package ANSYS® phase-depending materials models are not provided by default. To overcome this shortcoming so-called '*user programmable features*' can be used, which enable the user to include own materials models.

In summary one finds, that theoretical investigations of welding induced phase transformations concentrate, in most cases, on the resulting phase volume fractions. It is possible to estimate the distribution of hardness as well as the mechanical material behaviour,

---

[22] It is also possible to consider TRIP effects by adding an additional term $\underline{\underline{\varepsilon}}^{\mathrm{tr}}$.

| (A) | Defining the region of analysis |
|-----|-----|
| (A.1) | Defining and fine discretizing of an area at $X = L/2$ with normal vector parallel to the welding velocity. |
| (A.2) | Mapping of the calculated local temperature history of the 3D-mesh to the nodes of the area. |
| (A.3) | Saving the temporal temperature evolution at each node of the area. |
| **(B)** | **Heating period** |
| (B.1) | Definition of the initial phase composition ($\xi_0^M, \xi_0^{RA}, \xi_0^B, \xi_0^F$) by using experimentally obtained data. |
| (B.2) | Selection of all nodes with temperatures higher than $Ac3$; definition of $\xi^A = 1$ and $\xi^{M,B,F} = 0$ for these nodes. |
| (B.3) | Selection of nodes with maximal temperature between $Ac1$ and $Ac3$ and linear interpolation as follows: $\xi^A = \xi_0^{RA} + T_{max}(1 - \xi_0^{RA})/(Ac3 - Ac1)$ and, correspondingly, $\xi^F = 1 - \xi_0^M - \xi_0^B - \xi_0^A$. |
| (B.4) | The remaining unselected nodes do not change the initial composition. |
| **(C)** | **Cooling** |
| (C.2) | Definition of the the resulting values of b.3 as initial condition. |
| (C.3) | Calculation of the M- and A-volume fractions by means of Eq. (43). |
| (C.4) | Finally, the lateral phase distribution, representing the composition for arbitrary $X$ follows ( (any boundary effects are neglected). |

Table 4. Possible strategy to calculate the Martensite (volume) fraction following from heating and cooling during laser welding.

if - and only if - stress-strain relations (depending on the current phase composition) are available. Furthermore the local micro-morphology (size and shape of phases) can be considered by phase field approaches or partially by the LEBLOND model. However, combining such calculations with thermal and mechanical welding simulations requires considerable computational power, in particular for 3D geometries.

## 6.2 Hydrogen diffusion and local embrittlement

Hydrogen strongly decreases the mechanical strength (called hydrogen-induced embrittlement, HE) of steels and represents one of the most reasons for failure, (Timmins et al., 1997)[23]. Due to different manufacturing steps, such as annealing or electrolytic galvanizing, little contents of hydrogen are found within the material (0.5 - 3 ppm). Internal H-transport is characterized by interstitial diffusion; additionally, H is increasingly attracted at so-called 'traps', i.e. internal defects, such as precipitates, voids, phase boundaries or dislocations. Trapped hydrogen remains in the atomic state (H) or can recombine to $H_2$ under certain conditions. The traps act as potential wells, i.e. regions, in which hydrogen have a lower energetic state than at interstitial sites.

As the consequence of trapping, different diffusion coefficients are measured during charging and discharging of steels with H. During charging, first, all traps are filled before purely interstitial, stationary diffusion occurs, whereas during discharging normally only interstitial hydrogen escapes; the trapped hydrogen remains and do not contribute to the diffusion process, (Darken & Smith, 1949). Therefore the use of the 2nd FICKian law, $\partial_t c + \underline{\nabla} \cdot (\underline{\underline{D}} \cdot$

---

[23] The authors note that HE provokes annual costs of more than 100 billion U.S.$ within the U.S. industry.

$\underline{\boldsymbol{\nabla}} c) = 0$ ($\underline{\mathbf{D}}$: diffusion coefficient, $c$: H-atoms per unit volume[24]), is limited to some rare cases (e.g. to steels with saturated traps resulting from low density of defects or high H-content). In fact, a source term must be added to the right side of the equation, which was firstly developed by McNABB and FOSTER, (McNabb & Foster, 1963), and later by ORIANI assuming 'local equilibrium', (Oriani, 1970). Thus, the following equations hold for diffusion of hydrogen under the presence of local stress fields ($c << 1$), (Serebrinsky et al., 2004):

$$\mu(T, c) = \mu_0(T) + RT \ln(c) - \frac{\text{Tr}\,\underline{\underline{\boldsymbol{\sigma}}}}{3} V_{\text{H}} , \tag{45}$$

$$\frac{\partial c_{\text{L}}}{\partial t} + \underline{\boldsymbol{\nabla}} \cdot \underline{\boldsymbol{J}} = \frac{\partial c_{\text{T}}}{\partial t} , \quad (c = c_{\text{T}} + c_{\text{L}}) , \tag{46}$$

$$\underline{\boldsymbol{J}} = -\underline{\underline{\mathbf{M}}}(c) \cdot \left[ \underline{\boldsymbol{\nabla}} \mu \right] , \tag{47}$$

$$\underline{\boldsymbol{\nabla}} \mu = \frac{\partial \mu}{\partial T} \underline{\boldsymbol{\nabla}} T + \frac{\partial \mu}{\partial c} \underline{\boldsymbol{\nabla}} c + \frac{\partial \mu}{\partial p} \underline{\boldsymbol{\nabla}} p . \tag{48}$$

Here the following notation is used. $c_{\text{L}}$ and $c_{\text{T}}$: atomic concentration at interstitial or trap sites; $\mu$ and $\mu_0$: molar chemical potential of hydrogen within the 'binary' mixture hydrogen/steel and the temperature-depending, pure substance contribution at reference pressure $p = 0$; $p = \text{Tr}(\underline{\underline{\boldsymbol{\sigma}}}/3)$: hydrostatic stresses (pressure); $V_{\text{H}}$: molar volume of H in solid solution; $\underline{\underline{\mathbf{M}}} = c\,M\,\underline{\underline{\mathbf{I}}}$: mobility of H with $M = D/(\partial \mu / \partial c) = D/(RT)$, ($D$: diffusion coefficient); $R = 8.314$ J/mol K: universal gas constant and $\underline{\mathbf{J}}$: diffusion flux of H.

For the source term of the right hand side of Eq. (46) holds by statistical argu-ments, (Krom & Bakker, 2000):

$$\frac{\partial c_{\text{T}}}{\partial t} = N_{\text{T}} \frac{\partial \Theta_{\text{T}}}{\partial t} = N_{\text{T}} \left[ a\,\Theta_{\text{L}}(1 - \Theta_{\text{T}}) - b\,\Theta_{\text{T}} \right] , \tag{49}$$

and for equilibrium, where time derivatives will vanish:

$$\frac{\Theta_{\text{T}}}{\Theta_{\text{L}}(1 - \Theta_{\text{T}})} = \frac{a}{b} = \exp \left[ -\Delta E_{\text{T}}/RT \right] \equiv K_{\text{T}} , \tag{50}$$

with two constants, $a$ and $b$, which characterize the transition $L \to T$ and $T \to L$. Furthermore $N_{\text{T}}, \Theta_{\text{T}}$ denote the (constant) total trap number and the trap occupancy; $N_{\text{L}}, \Theta_{\text{L}}$ stands for the total number of interstitial sites and the corresponding occupancy; and $\Delta E_{\text{T}}$ identifies the energy difference between a trapped H-particle and an interstitial atom.

By inserting the relations $\Theta_{\text{L}} = c_{\text{L}}/N_{\text{L}}$ and $\Theta_{\text{T}} = c_{\text{T}}/N_{\text{T}}$ into Eq. (50) we obtain:

$$c_{\text{T}} = N_{\text{T}} \left( 1 + \frac{N_{\text{L}}}{K_{\text{T}} c_{\text{L}}} \right)^{-1} \tag{51}$$

and finally ($V_{\text{H}} = \text{const}, T = \text{const}$):

$$\frac{\partial c_{\text{L}}}{\partial t} + \underline{\boldsymbol{\nabla}} \cdot \left[ -D\,\underline{\boldsymbol{\nabla}} c_{\text{L}} + \frac{D V_{\text{H}}}{RT}(c_{\text{L}} \cdot \underline{\boldsymbol{\nabla}} p + p\,\underline{\boldsymbol{\nabla}} c_{\text{L}}) \right] = \frac{\partial}{\partial t} \left[ N_{\text{T}} \left( 1 + \frac{N_{\text{L}}}{K_{\text{T}} c_{\text{L}}} \right)^{-1} \right] . \tag{52}$$

---

[24] By convenience, we will call $c$ the concentration.

Equation (52) represents an evolution equation for the unknown quantity $c_L$. The required, materials data for $N_L, N_T, \Delta E_T$, which stand for a specific trap configuration, can be found in literature, (Krom & Bakker, 2000; Maroef et al., 2002; Oriani, 1970). In particular the trap density - and thus the total number of traps $N_T$ - increases with degree of cold-working. Furthermore the (residual) hydrostatic stresses, $p = \frac{1}{3}\mathrm{Tr}(\underline{\sigma})$, occur in the above equation, which are known as result of the presented welding simulations, see paragraph 4.2 and Figure 32. By means of suitable numerical framework, such as the method of Finite Differences, equation (52) can be solved. Therewith predictions about the hydrogen distribution within the material can be made following from the specific laser welding procedure. In Figure 33 different contourplots are displayed, which show - exemplarily -
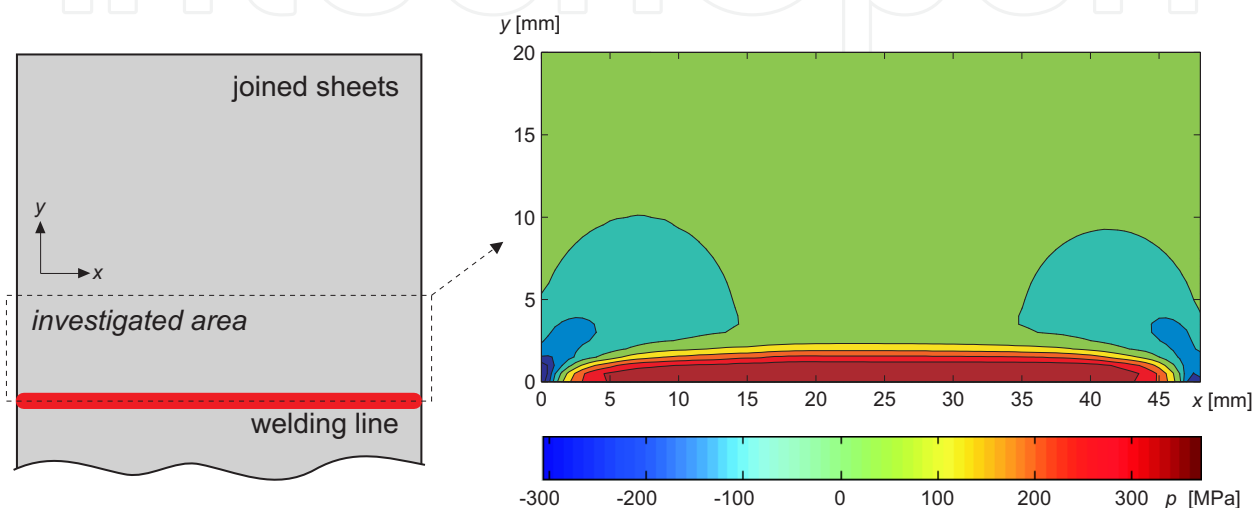


Fig. 32. Illustration of the analyzed region and the calculated, residual hydrostatic stresses used as input data to solve Eq. (52) numerically.

the temporal evolution of hydrogen after laser welding as investigated in Section 4. Here we neglect - as a first approximation - the right hand side of Eq. 52, so that the diffusible hydrogen amount is exclusively investigated (no un-/trapping, $D = 5.8 \cdot 10^{-4}$ mm$^2$/s). Moreover, a uniform $96 \times 40$ ( length $\times$ width) grid is used in combination with NEUMANN boundary conditions ($\underline{J}_{\partial\Omega} = 0$). A finite difference scheme as well as an EULER time-step scheme is implemented in order to numerically solve the above diffusion equation. Furthermore the spatial distribution of the hydrostatic stresses, calculated by the preliminary welding simulations, is applied to predict hydrogen transport due to local mechanical stress fields.

Obviously, residual stresses lead to the redistribution of hydrogen. In particular, H is increased found in regions of tensile stresses (positive strains), whereas domains of compressive stresses (negative strains) show reduced hydrogen concentrations. The final concentration profile (equilibrium) is determined by the maximal hydrostatic stresses and is found after ~15 h. Furthermore the long-time simulations (12 h, 30 d) indicate, that the homgeneous hydrogen concentration far from welding also decreases due to the H-accumulation in the welding line ($c_{homog}(t = 30d) \approx 0.46$). On the other hand the hydrogen concentration near the joining region already increases after eight minutes from 0.5 ppm to 0.52 ppm. However, the present simulations only allow for a rough reproduction of H-diffusion during and after welding. Particularly, the heat input reactivates trapped hydrogen in the vicinity of the joining region, which may drastically increase the diffusible amount. Considerable concentration gradients could result, which are additionally promoted
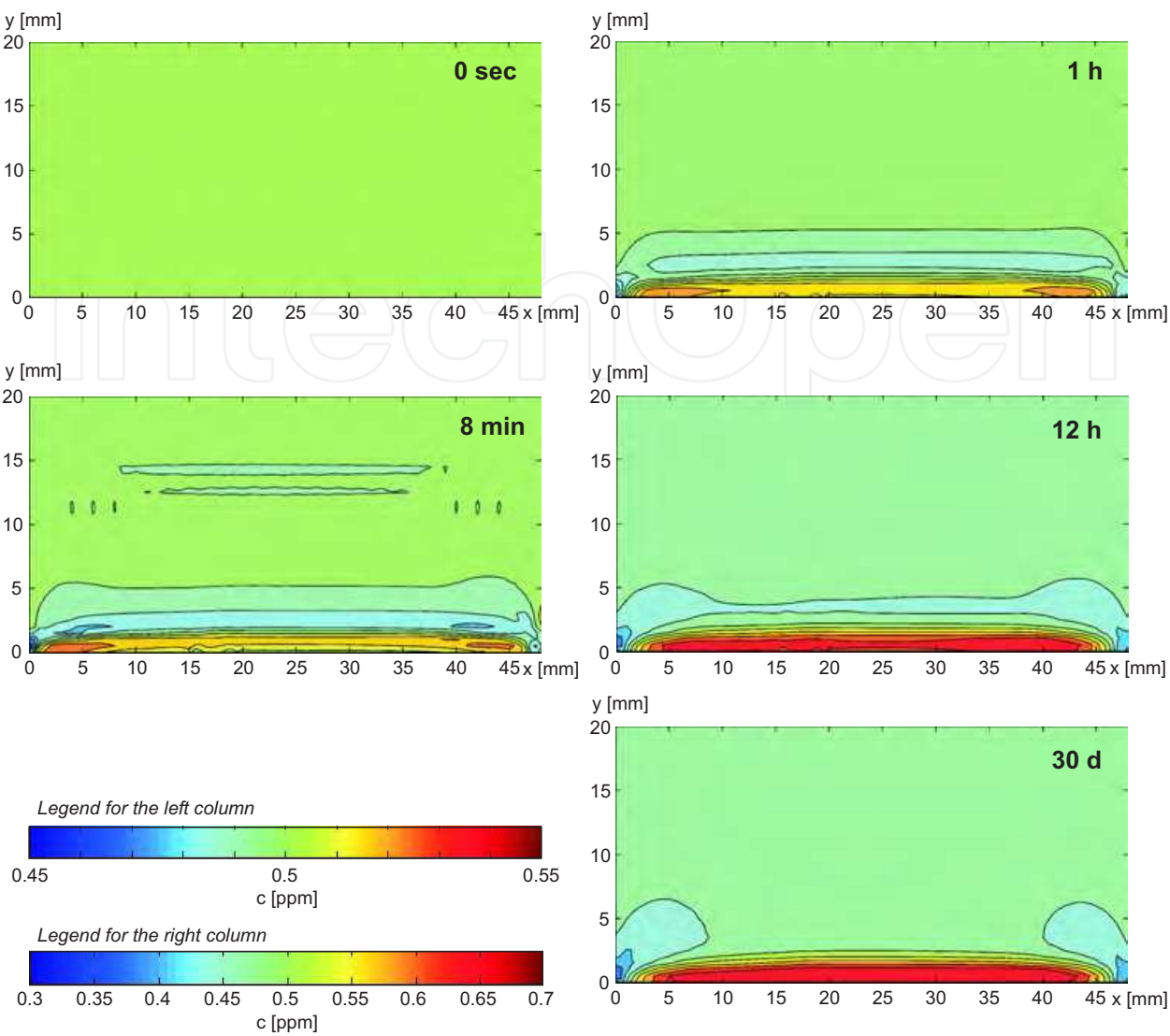
Fig. 33. Predicted evolution of the local hydrogen concentration in the vicinity of the welding line. Initial, homogeneous hydrogen concentration: 0.5 ppm.

by successive H-diffusion to regions of high residual stresses. This phenomenon may lead to significant local H-concentrations and to fatal embrittlement. Moreover, boundary conditions, such as air moisture and hydrogen within (Zn-)coatings can emphasize this effect, which, nevertheless, causes failure like e.g. cold cracking. Such defects often occur within the bulk of the material and, therefore, are not visible to the naked eye. Here theoretical simulations can help to identify domains of increased failure sensitivity.

### 6.3 Coupling of weld-pool-dynamics calculations and solid state FE-analysis

A crucial precondition for the above illustrated FE-investigation is the a priori knowledge of the weld pool geometry. However, local temperature distribution and resulting varying surface tension (additionally influenced by steel composition, e.g. S and N content) directly effect the weld pool flow conditions, (Mills et al., 1998). Therefore, varying process parameter

as well as different steel grades may lead to considerable changes of the weld pool geometries, primarily w.r.t. thickness and depth.

In particular the weld pool depth is a priori defined by the parameter $z^{(2/3))}$ (LASIM makro provided by ANSYS®) or by $f_i$ (GAUSSian distribution). In order to cancel this assumption simulations are desirable, which - depending on the heat input - consider the melting process (and eventually the vaporization) and weld pool dynamics, i.e. the solid-liquid system (and eventually the liquid-vapour system). Then, the resulting temperature distribution can be used in a separate solid state FE-simulation to calculate the mechanical response, i.e. residual stresses or distortions.

Starting point of most computational fluid dynamics (CFD) simulations is the NAVIER-STOKE equation. This equation directly follows by considering the balance of momentum, Eq. (2), and the following constitutive law for the stress tensor:

$$\underline{\sigma} = -p\,\underline{I} + \nu \mathrm{Tr}(\boldsymbol{\nabla}\,\mathbf{v})_{\mathrm{sym}}\,\underline{I} + 2\mu(\boldsymbol{\nabla}\,\mathbf{v}) \; . \tag{53}$$

The symbols $p, \nu, \mu$ identify pressure, kinematic and shear viscosity. Furthermore the index $(\cdot)_{\mathrm{sym}}$ stands for the symmetric part of velocity gradient.

At this point we present various conceptual studies for illustrating the coupling between CFD- and FE-simulations. For this reason we use the CFD-software package ANSYS CFX® as well as the FE-software ANSYS® classic. By considering the welding process, the transition point between solid and liquid is defined by the rapid, jump-wise change of the temperature-depending material data for:

- dynamic viscosity $\eta = \nu/\rho$,
- specific heat capacity $c_{\mathrm{p}}$,
- heat conductivity $\kappa$ and
- mass density $\rho$.

The transition between the liquid and gaseous state must be also specified, especially to realistically model the free surface melt/air (e.g. the melt pool curvature). For this reason we define a volume of Length×Width×Heigh = L×W×H= $50 \times 35 \times 26.5$ mm (half model), consisting of the steel sheet (L×W×H = $50 \times 35 \times 1.5$ mm), the air above (H=20 mm) and the air below (H=5 mm). After meshing the materials properties must be assigned to each element in order to define the different materials within the volume. Here - as a first approximation - constant standard values are used for the elements representing the air. Such element-wise assignment can be realized by the definition of element-specific volume fractions (and partial pressures). It holds:

$$\Xi_{\mathrm{iron}}(h) = \begin{cases} 1 & \text{if} & -1.5 \leq h \leq 0 \\ 0 & \text{if} & h < -1.5 \quad \text{or} \quad h > 0 \end{cases} . \tag{54}$$

and vice versa for $\Xi_{\mathrm{air}}(h)$. Note, that the origin of the coordinate system in Eq. (54) is defined a the upper surface of the metallic sheet. Within the thin boundary volume between liquid and air, in which a linear interpolation is performed between the jump-wise changing properties, the heat is supplied via the GAUSSian distribution ($\sigma = 1.4$ mm, $P = 0.5\,\eta\,P_0 = 843$ W). Here the centre of distribution changes according to the welding velocity $v_{\mathrm{s}} = 0.625$ m/min. Figure

34 and 35 (1st row) illustrate the calculated melt pool geometry (including main flow lines) as well as the resulting temperature distribution within the steel sheet (for $t = 2.1$ s).

In order to couple CFD- and FE-analysis *in one direction* the following strategy is applied: **(a)** The temperature distribution of the steel sheet, resulting from the CFD-simulation, is mapped to a new mesh (mostly with larger element size), which will be later used in the FE-analysis. **(b)** The mapped temperatures of the steel sheet are exported to data files for each time step; **(c)** The mechanical FE-analysis (calculation of stresses and strains) is performed by reading the temperatures from the corresponding data files for each time step.

Figure 35 (2nd row, left) shows the imported temperature distribution in ANSYS® classic accordingly to the results of ANSYS CFX® in Figure 35 (1st row). The lower right panel of Figure 35 represents the results of the mechanical FE-simulation (distortions are amplified by factor 5). Here the mechanical boundary condition is chosen such, that all nodes of the upper and lower side at $x = W/2$ are fixed ($\underline{u} = 0$). Furthermore, the discretization of the mesh is obviously chosen too large. Thus inaccurate stresses are obtained in some regions, which are justifiable due to the conceptual character of the study. Moreover, the laser-welding specific phenomenon of keyhole formation is not considered within the above explained CFD-analysis. Therefore the presented strategy is more appropriate for 'classical' welding processes, such as TIG-, MIG-, or MAG welding. Nevertheless, the results clearly show the potential for coupling weld-pool-dynamics simulations with solid state FE-analysis.
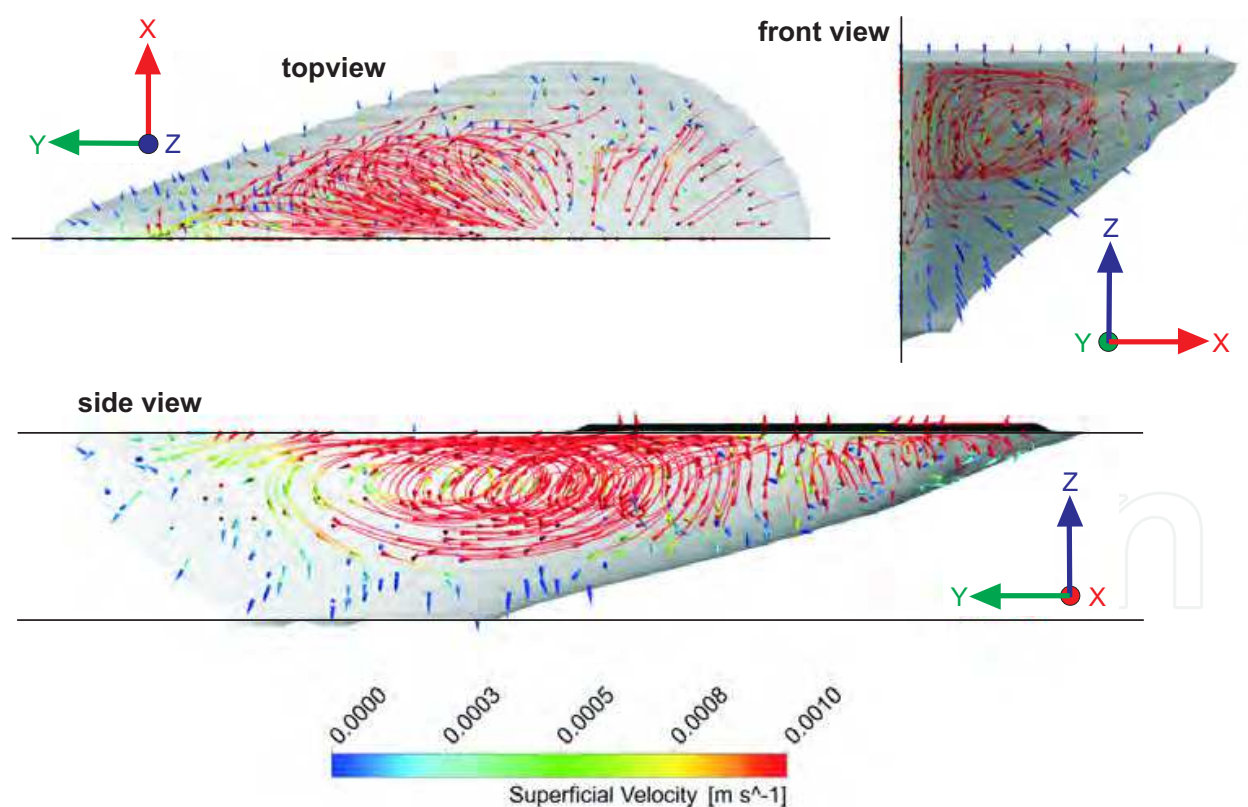


Fig. 34. Weld pool geometry and main flow lines calculated by ANSYS CFX®. Clearly to see is the MARANGONI convection due to the temperature-depending surface tension, (Lee et al., 1998).
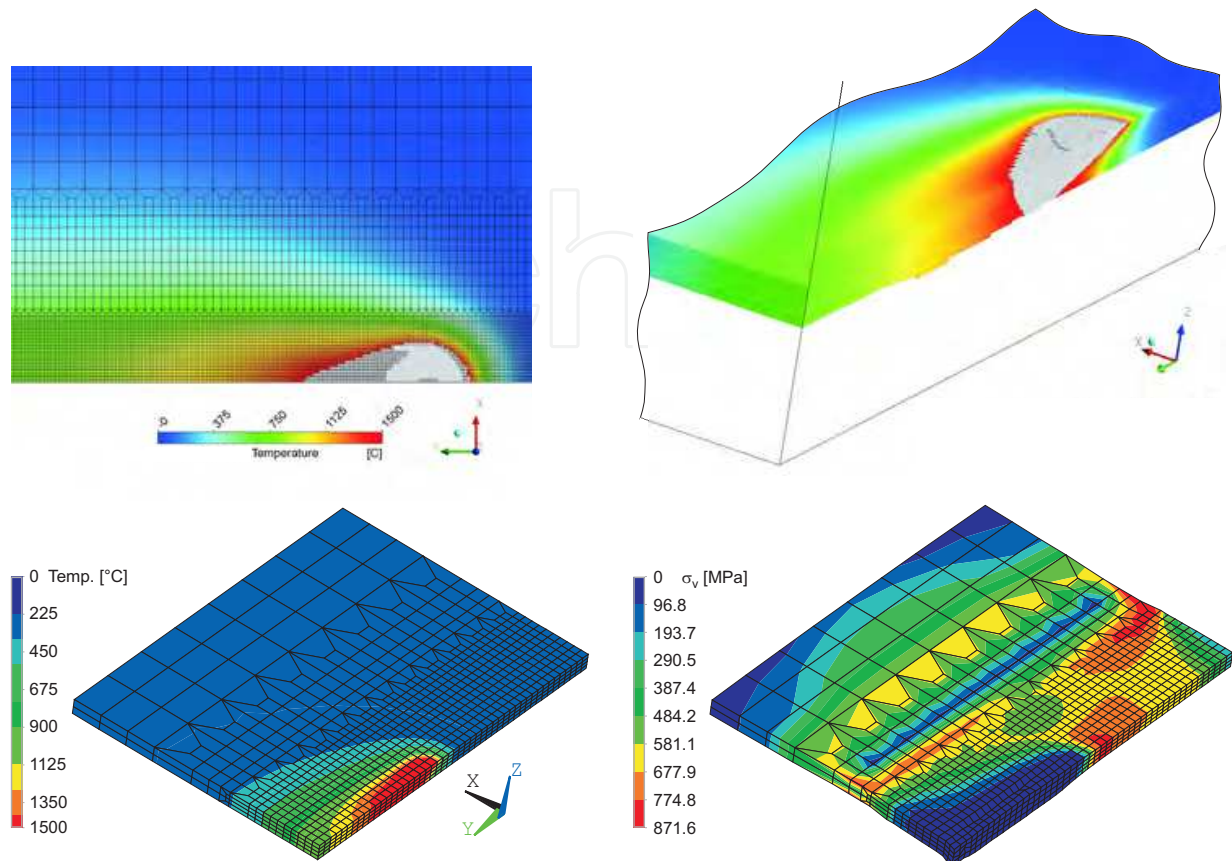
Fig. 35. *1st row*: Temperature distribution calculated with ANSYS CFX®. Here the moving heat source is applied within the boundary layer air/steel. *2nd row (left)*:Temperature distribution imported from CFX® to ANSYS® classic. *2nd row (right)*: Calculated VON MISES stress distribution during welding.

## 7. Conclusion and summary

In the present work the laser welding process, usually found during continuous manufacturing of steels, was investigated from the experimental and numerical point-of-view. We restricted to the example of multiphase, as-rolled steels and presented the following items in detail:

1. Explanation of the continuum mechanical and thermodynamical framework required for modelling of welding;

2. Introduction into the mathematical, numerical framework typically used for FE-simulations;

3. Derivation of all required materials data, including experimental testing and optimization by minimizing the mean-square deviation;

4. Presentation of thermal and mechanical FE-simulations of the laser welding process for TRIP 700 (as-rolled state);

5. Performing of welding experiments and comparison of the experimental and theoretical results; and

6. Discussion of continuative, welding-related phenomena and tasks for future investigations.

Great importance is attached to the determination of required materials data, since simulations can only be as reliable as the underlying input data. Here all caloric materials data were taken from literature or databases. Only mechanical data, in particular temperature depending stress-strain curves, are rarely available. Therefore one-dimensional tensile tests were performed at different temperatures by using the Gleeble3500 equipment.

All simulations were realized by means of the FE-program package ANSYS®. For the experimental investigations material were removed from production and joined at the laser test bench under manufacturing conditions. The comparison of the experimental and theoretical results shows partially excellent agreements; only the calculated lateral distortions are overestimated but also qualitative reproduce the experimental curve. Phase transformations during welding are not considered within the simulations. Although micro-structural changes do not appear to strongly influent the mechanical response of TRIP 700, this phenomenon is worthy to model in future work. Especially, the finite cooling time during welding lead to a shift of jumps of the (stationary) curves in Figure 10. Additionally micro-morphological changes (e.g. grain coarsening within the HAZ) and partial trans-formations occur. These changes may not affect the mechanical response but yield modified materials properties, such as loss of hardness, which could be relevant for subsequent materials processing.

## 8. Appendix: Thermal boundary conditions

### A. Radiation and natural convection

We start with the established relation for heat transfer via convection over the boundary of the body:

$$\underline{\mathbf{q}}_n = \alpha A (T - T_0) \cdot \underline{\mathbf{n}} . \tag{A1}$$

For radiation the heat transfer is quantified by the STEFAN-BOLTZMANN law, viz.:

$$\underline{\mathbf{q}}_S = \sigma_{\text{SB}} \epsilon A (T^4 - T_0^4) \cdot \underline{\mathbf{n}} . \tag{A2}$$

By combining the equations one relation for both effects follows, which contains an effective heat transfer coefficient $\alpha_{\text{eff}}$:

$$\underline{\mathbf{q}}_{n,\text{tot}} = \underline{\mathbf{q}}_n + \underline{\mathbf{q}}_S = \alpha_{\text{eff}}(T) A (T - T_0) \cdot \underline{\mathbf{n}} \quad , \quad \alpha_{\text{eff}}(T) = (\alpha + \sigma_{\text{SB}} \epsilon) \frac{T^4 - T_0^4}{T - T_0} \tag{A3}$$

with $\alpha = 5.0$ W/(m$^2$K): convective heat transfer coefficient[25]; $\sigma_{\text{SB}} = 5.67 \cdot 10^{-8}$ W/(m$^2$K$^4$): STEFAN-BOLTZMANN constant; $\epsilon = 0.5$: emission coefficient[25]; $A$: area of radiation; $\underline{\mathbf{n}}$: normal vector; $T_0$: reference temperature.

---

[25] These values are ad-hoc assumed according to standard literature.

### B. Forced convection

Figure 25 (left) illustrates the supply of shielding gas (Helium) via a capillary tube contrary to the joining direction during welding. By assuming a setting angle of $\alpha = 45°$, tube diameter of $D = 1.8$ mm and the typical volume flux of $\dot{V} = 10$ l/min the following Helium velocity parallel to the sheet surface result, see also Figure 36:

$$v_x = v_s \sin(\alpha) = \frac{4\dot{V}}{\pi D^2} \sin(\alpha) = 46.3 \,\text{m/s} . \tag{A4}$$

By means of the kinematic viscosity $\nu = 104.5$ mm$^2$/s (Helium), the characteristic length $L = 50$ mm, the conductibility of temperature $a = 153 \cdot 10^{-6}$ m$^2$/s and the heat conductivity of fluid $\kappa_{\text{He}} = 0.14$ W/(mK) the following dimensionless numbers hold:

$$\text{Re} = \frac{v_x L}{\nu} = 22.2 \quad \text{and} \quad \text{Pr} = \frac{\nu}{a} = 0.68 . \tag{A5}$$

The REYNOLDS number Re characterizes the turbulent behaviour of the fluid flow, whereas the PRANDTL number describes the thickness of the temperature boundary layer. In the present case laminar conditions hold; consequently we use the relation, (Grothe & Feldhusen, 2007):

$$\text{Nu} = \frac{\alpha L}{\lambda} = 0.332 \sqrt{\text{Re}} \sqrt[3]{\text{Pr}} . \tag{A6}$$

By using Eq. (A6) the modified heat transfer coefficient $\alpha = 2300$ W/(m$^2$K) directly follows. This value holds for the joining regions at the upper surface during welding. During cooling the supply of yielding gas is cancelled, thus natural convection including radiation takes place, cf. Figure 36.
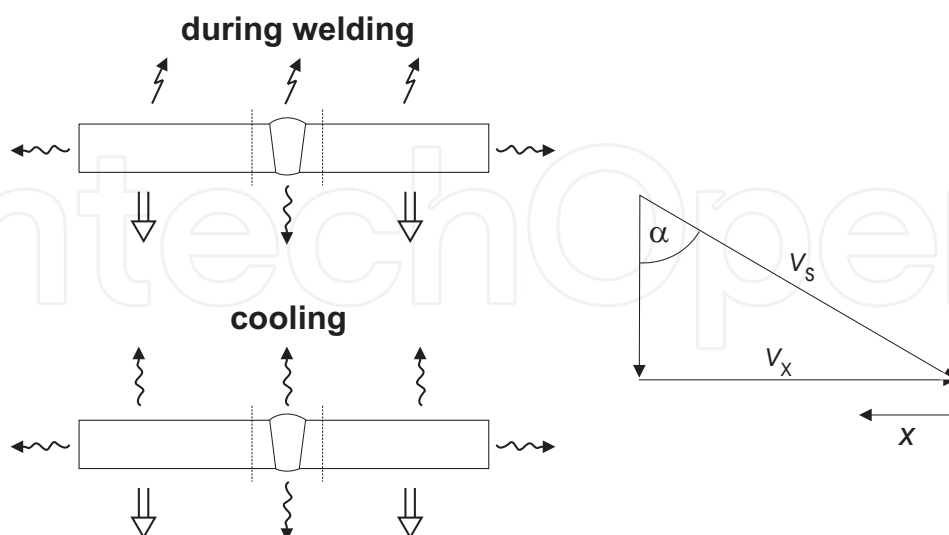


Fig. 36. Different thermal boundary conditions during welding and cooling (the used symbols are explained in Figure 8). *Right*: velocity triangle to determine the parallel contribution $v_x$.

## C. Heat conduction by thermal contact

Beyond the lateral distance from the welding seam of $3 - 4$ mm the lower side of the sheet lies on a steel surface. Thus the thermal contact steel-to-steel must be considered. Such situation is typically described within the literature by means of the quantity of Thermal Contact Resistance, $R_{TC}$, or conductance, $C_{TC}$. The following relation holds:

$$\underline{\mathbf{q}} = \frac{A\,\Delta T}{R_{TC}} \cdot \underline{\mathbf{n}} \quad \text{and} \quad C_{TC} = \frac{1}{R_{TC}} \,. \tag{A7}$$

Values for $C_{TC}$ and $R_{TC}$ can be found in literature for typical materials combinations, but note, there is a strong dependence to the contact pressure. Obviously the heat transfer coefficient $\alpha$ can be directly replaced by $C_{TC}$ in case of thermal contact. Based on (Shojaefard & Goudarzi, 2008) the following value is used in the simulations:

$$R_{TC} = 0.33\,\frac{\text{m}^2\text{K}}{\text{kW}} \quad \Rightarrow \quad \alpha = \frac{1}{R_{TC}} \approx 3000\,\frac{\text{W}}{\text{m}^2\text{K}} \,. \tag{A8}$$

## 9. Acknowledgement

## 10. References

ANSYS® Release 11.0 SP1 (2007). Copyright SAS IP Inc., Canonsburg.

ANSYS Inc. (2007). *Theory Reference for ANSYS and ANSYS Workbench*. ANSYS Release 11.0, SAS IP Inc., Canonsburg.

Avrami, M. (1939). Kinetics of Phase Change. I General Theory. *J. Chem. Phys.*, Vol. 7, 1103–1112.

Avrami, M. (1940). Kinetics of Phase Change. II Transformation-Time Relations for Random Distribution of Nuclei, *J. Chem. Phys.*, Vol. 8, 212–224.

Barth, G. & Groß, U. (2004). *Untersuchung der thermophysikalischen Stoffeigenschaften von Stahl bei Temperaturen bis zu 1600 °C*, report of the TU Bergakademie Freiberg, Freiberg, Germany.

Cahn, J.W. & Hilliard, J.E. (1958). Free energy of a Nonuniform System. I. Interfacial Free Energy. *J. Chem. Phys.*, Vol. 28, No. 2, 258–267.

Cahn, J.W. (1961). On Spinodal Decomposition. *Acta Metall.*, Vol. 9, 795–801.

Darken, L.S. & Smith, R.P. (1949). Behavior of hydrogen in steel during and after immersion in acid. *Corrosion*, Vol. 5, 1–16.

De, A.; Maiti, S.K.; Walsh, C.A. & Bhadeshia, H.K.D.H. (2003). Finite element simulation of laser spot welding. *Sci. Technol. Weld. Joi.*, Vol. 8, No. 5, 377–384.

Dean, D.; Yu, L.; Hisashi, S.; Masakazu, S. & Hidekazu, M. (2003). Numerical simulation of residual stress and deformation considering phase transformation effect. *Trans. JWRI*, Vol. 32, No. 2, 325–333.

Dean, D. & Hidekazu, M. (2006). Prediction of welding residual stress in multi-pass butt-welded modified 9Cr-1Mo steel pipe considering phase transformation effects. *Comp. Mater. Sci.*, Vol. 37, 209–219.

Dean, D.; Hidekazu, M. & Wei, L. (2008). Numerical and experimental investigations on welding residual stress in multi-pass butt-welded austenitic stainless steel pipe. *Comp. Mater. Sci.*, Vol. 42, 234–244.

Dean, D. & Hidekazu, M. (2008). Finite element analysis of temperature field, microstructure and residual stress in multi-pass butt-welded 2.25Cr-1Mo steel pipes. *Comp. Mater. Sci.*, Vol. 43, 681–695.

DIN EN 10002-1 (2001). Zugversuch Teil 1: Prüfverfahren bei Raumtemperatur. Deutsches Institut für Normung e.V., Beuth Verlag GmbH, Berlin.

Dong, Z.B. & Wei, Y.H. (2008). Three dimensional modeling weld solidification cracks in multipass welding. *Theor. Appl. Fract. Mech.*, Vol. 46, 156–165.

Elmer, J.W.; Wong, J. & Ressler, T. (2001). Spatially Resolved X-Ray Diffraction Mapping of Phase Transformations in the Heat-Affected Zone of Carbon-Manganese Steel Arc Welds. *Metall. Mater. Trans. A*, Vol. 32A, 1175–1187.

Fan, H.G. & Kovacevic, R. (1999). Droplet formation, detachment, and impingement on the molten pool in gas metal arc welding. *Metall. Mater. Trans. B*, Vol. B30, 791–801.

Feldmann, C. (2008). *Thermoelemente*, talk manuscript, University of Applied Scienes and Arts Dortmund, url: http://ln.iuk.fh-dortmund.de/˜gebhard/STA/vortraege/ (last access: Mai 2011).

Francis, J.A.; Bhadeshia, H.K.D.H. & Withers, P.J. (2007). Welding residual stresses in ferritic power plant steels. *Mater. Sci. Tech. Ser.*, Vol. 23, No. 9, 1009–1020.

Gross, D. & Seelig, T. (2006). *Fracture Mechanics*, Springer, ISBN: 978-3-540-37113-7, Berlin Heidelberg New York.

Grothe, K.-H. & Feldhusen, J. (2007). *Dubbel Taschenbuch für den Maschinenbau*, 22nd edition, Springer, ISBN 978-3-540-49714-1, Berlin Heidelberg New York, page D32 ff..

Hemmer, H. & Grong, Ø. (1999). A process model for the heat-affected zone microstructure evolution in duplex stainless steel weldments: Part I. the model. *Metall. Mater. Trans. A*, Vol. 30A, 2915–2929.

Hemmer, H.; Grong, Ø & Klokkehaug, S. (2000). A process model for the heat-affected zone microstructure evolution in duplex stainless steel weldments: Part II. Application to electron beam welding *Metall. Mater. Trans. A*, Vol. 31A, 1035–1048.

JMatPro 6.0. (2011), Sente Software Ltd., Surrey Technology Centre, 40 Occam Road, GU2 7YG, United Kingdom.

Junk, A. & Groth, C. (2004). Schweißprozesssimulation mit dem SST, Integration neuer Ansätze und bewährter Teilmodelle in die FE-Simulation des Laserstrahlschweißens. *Proceedings of the 22nd CAD-FEM Users' Meeting*, 13 pages, ISBN: 3-937523-01-4, Dresden, November 2004, CADFEM, Grafing.

Modeling, Simulation and Experimental Studies of Distortions,
Residual Stresses and Hydrogen Diffusion During Laser Welding of As-Rolled Steels

121

Kang, S.-H. & Im, Y.-T. (1987). Three dimensional thermo-elastic-plastic finite element modeling of quenching process of plain-carbon steel in couple with phase transformation. *Int. J. Mech. Sci.*, Vol. 49, 423–439.

Khiabani, A.C. & Sadrnejad, S.A. (2009). Finite element evaluation of residual stresses in thick plates *Int. J. Mech. Mater. Des.*, Vol. 5, No. 3, 253–261.

Ki, H.; Mohanty, P.S. & Mazumder, J. (2002). Modeling of laser keyhole welding: Part I. mathematical modeling, numerical methodology, role of recoil pressure, multiple reflections, and free surface evolution. *Metall. Mater. Trans. A*, Vol. 33A, No. 6, 1817–1830.

Ki, H.; Mohanty, P.S. & Mazumder, J. (2002a). Modeling of laser keyhole welding: Part II. simulation of keyhole evolution, velocity, temperature profile, and experimental verification. *Metall. Mater. Trans. A*, Vol. 33A, No. 6, 1831–1842.

Koistinen, D.P. & Marburger, R.E. (1959). A general equation prescribing the extent of the austenite-martensite transformation in pure iron-carbon alloys and plain carbon steels. *Acta Metall.*, Vol. 7, 59–60.

Komanduri, R. & Hou, Z.B. (2000). Thermal Analysis of the Arc Welding Process: Part I. General Solutions. *Metall. Mater. Trans. B*, Vol. 31B, 1353–1370.

Kotowski, J. (1998). *Experimentelle und numerische Ermittlung der Energieeinkopplung während des Laserstrahlschweiß¡ens von Tailored Blanks*, diploma thesis, TU Braunschweig.

Krom, A.H.M. & Bakker, A.D. (2000). Hydrogen Trapping Models in Steel. *Metall. Mater. Trans. B*, Vol. 31B, 1475–1482.

Leblond, J.B. & Devaux, J. (1984). A new kinetic model for anisothermal metallurgical transformations in steels including effect of austenite grain size. *Acta Metall.*, Vol. 32, No. 1, 137–146.

Lee, P.D.; Quested, P.N. & McLean, M. (1998). Modelling of Marangoni Effects in Electron Beam Melting. *Phil. Trans. R. Soc. Lond. A*, Vol. 356, 1027–1043.

Maroef, I.; Olson, D.L.; Eberhart, M. & Edwards, G.R. (2002). Hydrogen trapping in ferritic steel weld metal. *Int. Mater. Rev.*, Vol. 47, No. 4, 191–223.

McNabb, A. & Foster, P.K. (1963). A New Analysis of the Diffusion of Hydrogen in Iron and Ferritic Steels. *Trans. Metall. Soc. AIME*, Vol. 227, 618–627.

Mills, K.C.; Keene, B.J.; Brooks, R.F. & Shirali, A. (1998). Marangoni Effects in Welding. *Phil. Trans. R. Soc. Lond. A*, Vol. 356, 911–925.

Müller, I. (1984). *Thermodynamics*, Pitman Publishing Inc., ISBN: 0-273-08577-8, London.

Müller, I. (1999). *Grundzüge der Thermodynamik*, Springer (2nd edition), ISBN: 3-540-64703-1, Berlin Heidelberg New York.

Müller, I. & Müller, W.H. (2009). *Fundamentals of Thermodynamics and Applications*, Springer, ISBN: 978-3-540-74645-4, Berlin Heidelberg.

Oriani, R.A. (1970). The diffusion and trapping of hydrogen in steel. *Acta Metall.*, Vol. 18, 147–157.

Ossenbrink, R. & Michailov, V. G. (2007). *Thermomechanical Numerical Simulation with the Maximum Temperature Austenisation Cooling Time Model (STAAZ)*, in: Mathematical Modelling of Weld Phenomena 8 (ed. Cerjak, H.H.), Verlag der Technischen Universität Graz, Graz (Austria), ISBN: 978-3-902465-69-6, 357–372.

Ossenbrink, R. (2008). *Thermomechanische Schweißsimulation unter Berücksichtigung von Gefügeumwandlungen*, PhD thesis, Brandenburg University of Technology, Shaker Verlag, ISBN: 978-3-8322-8131-1, Aachen.

Phanikumar, G.; Dutta, P. & Chattopadhyay, K. (2004). Computational modeling of laser welding of Cu-Ni dissimilar couple. *Metall. Mater. Trans. B*, Vol. 35B, No. 2, 339–350.

Pfeiffer, S. & Schulz, W. (2009). Structural validation of different approaches for the modelling of welding distortion of steel-based parts. Final Report, project no. P708, FOSTA - Forschungsvereinigung Stahlanwendung e.V., Düsseldorf.

Richter, F. (1973). *Die wichtigsten physikalischen Eigenschaften von 52 Eisenwerkstoffen*. Mitteilungen aus dem Forschungsinstitut der Mannesmann AG, Stahleisen - Sonderberichte, Heft 8, Stahleisen Dï£¡sseldorf m.b.H., Düsseldorf.

Serebrinsky, A.; Carter, E.A. & Ortiz, M. (2004). A quantum-mechanically informed continuum model of hydrogen embrittlement. *J. Mech. Phys. Solids*, Vol. 52, 2403–2430.

Shojaefard, M.H. & Goudarzi, K. (2008). The Numerical Estimation of Thermal Contact Resistance in Contacting Surfaces. *American Journal of Applied Sciences*, Vol. 5, No. 11, 1566–1571.

Sloan, S.W. (1987). Substepping schemes for the numerical integration of elastoplastic stress-strain relations. *Int. J. Numer. Meth. Eng.*, Vol. 24, 893–911.

Spina, R.; Tricarico, L.; Basile, G. & Sibillano, T. (2007). Thermo-mechanical modeling of laser welding of AA5083 sheets. *J. Mater. Process. Technol.*, Vol. 191, 215–219.

Stouffer, D.C. & Dame, L.T. (1996). *Inelastic Deformations of Metals*, John Wiley & Sons Inc., ISBN: 0-471-02143-1, New York.

Thiessen, R.G.; Sietsman, J.; Palmer, T.A.; Elmer, J.W. & Richardson, I.M. (2007). Phase-field modelling and synchrotron validation of phase transformations in martensitic dual-phase steel. *Acta Mater.*, Vol. 55, 601–614.

Tian, Y.; Wang, C.; Zhu, D. & Zhou, Y. (2008). Finite element modeling of electron beam welding of a large complex Al alloy structure by parallel computations. *J. Mater. Process. Technol.*, Vol. 199, 41–48.

Timmins, P.F. (1997). *Solutions to Hydrogen Attack in Steels.* ASM International, Materials Park , OH (USA), ISBN: 0-87170-597-4.

Umemoto, M.; Horiuchi, K. & Tamura, I. (1982). Transformation Kinetics of Bainit during Isothermal Holding and Continuous Cooling. *Trans. Iron Steel Inst. Jpn.*, Vol. 22, 854–861.

Umemoto, M.; Horiuchi, K. & Tamura, I. (1983). Pearlite Transformation during Continuous Cooling and Its Relation to Isothermal Transformation. *Trans. Iron Steel Inst. Jpn.*, Vol. 23, 690–695.

Voss, O. (2001). *Untersuchung relevanter Einflussgrößen auf die numerische Schweißsimulation*, PhD thesis, TU Braunschweig, Shaker Verlag, ISBN: 3-8265-9119-4, Aachen.

Wang, Y.; Shi, Q. & Tsai, H.L. (2001). Modeling of the effects of surface-active elements on flow patterns and weld penetration. *Metall. Mater. Trans. B*, Vol. 32B, 145–161.

Wang, Y. & Tsai, H.L. (2001). Effects of surface active elements on weld pool fluid flow and weld penetration in gas metal arc welding. *Metall. Mater. Trans. B*, Vol. 32B, 501–515.

Wriggers, P. (2000). *Nichtlineare Finite-Elemente-Methoden*, Springer, ISBN: 3-540-67747-X, Berlin Heidelberg New York.

Zener, C. (1949). Theory of Growth of Spherical Precipitates from Solid Solution. *J. App. Phys.*, Vol. 20, 950–953.

Zhou J. & Tsai, H.L. (2008). Modelling of Transport Phenomena in Hybrid Laser-MIG Keyhole Welding. *Int. J. Heat Mass Transf.*, Vol. 51, 4353–4366.

**Materials Science and Technology**

Edited by Prof. Sabar Hutagalung

Materials are important to mankind because of the benefits that can be derived from the manipulation of their properties, for example electrical conductivity, dielectric constant, magnetization, optical transmittance, strength and toughness. Materials science is a broad field and can be considered to be an interdisciplinary area. Included within it are the studies of the structure and properties of any material, the creation of new types of materials, and the manipulation of a material's properties to suit the needs of a specific application. The contributors of the chapters in this book have various areas of expertise. therefore this book is interdisciplinary and is written for readers with backgrounds in physical science. The book consists of fourteen chapters that have been divided into four sections. Section one includes five chapters on advanced materials and processing. Section two includes two chapters on bio-materials which deal with the preparation and modification of new types of bio-materials. Section three consists of three chapters on nanomaterials, specifically the study of carbon nanotubes, nano-machining, and nanoparticles. Section four includes four chapters on optical materials.

**How to reference**

In order to correctly reference this scholarly work, feel free to copy and paste the following:

INTECH

open science | open minds